東北大学機関リポジトリ
TOUR
Tohoku University Repository
東北大学

The role of the extracellular impedance profiles in the multi-compartmental model for neurons: A unified formalism for recording and stimulation

著者	王　凱
学位授与機関	Tohoku University
URL	http://hdl.handle.net/10097/51127

修士論文

The role of the extracellular impedance profiles in the multi-compartmental model for neurons: A unified formalism for recording and stimulation

(神経細胞のマルチコンパートメントモデルにおける細胞外抵抗分布の役割：細胞外記録および細胞外電気刺激のための統一形式化)

東北大学大学院医学系研究科医科学専攻

脳機能開発研究分野

王　凱（A9MM5003）

Abstract

With the rapid increase in technologies to observe electric activity inside the brain, scientists have felt urged to create proper links between intracellular- and extracellular- based experimental approaches. Biophysical models at both physical scales have been formalized under assumptions that impede the natural creation of such links. In this work, we propose a novel theoretical framework to include the geometrical and electrotonic properties of neurons in a multi-compartment model that comprises four different devices, i.e. the integrator, the propagator, the 3D-connector and the collector. A clear distinction in the resistivity profiles of both the intracellular and extracellular spaces is made for these devices. We deduced the general equations for the membrane potential at the compartments in each device. In particular, we applied this framework to model the geometrical aspects of pyramidal cell layer 5 (PCL5). Our model was able to reproduce the decay and delay curves of back propagating APs in this type of cell with a better agreement to experimental data. We used the voltage drops of the extracellular resistances at each compartment to approximate the local field potentials generated by a single PCL5 in close proximity to the microelectrodes arrays. From the voltage drops produced by back-propagating APs, we were able to estimate current multipolar moments generated by a single PCL5. By adding external current sources in parallel to the extracellular resistances, for the first time, we were able to create a context to stimulate any type of neurons from microelectrodes arrays in close proximity, which incorporates dynamic reactivity from these types of excitable cells. We used such an extended framework to evaluate the profile of extracellular current injection needed to stimulate the PCL5. In our model, the actual kinetics for PCL5 ionic currents and the geometrical properties of these cells were included.

Key words: multi-compartment model, electrotonic, neuron, pyramidal cells, back-propagating APs

Introduction

Neuronal activity at the cellular level has been investigated in the past using two electrophysiological approaches. In the first one, individual neurons in situ/vitro are targeted with glass-microelectrodes using a variety of recording and preparation protocols. The whole-cell voltage/current clamp is considered the most classical recording protocol, and it is usually performed on acute slice preparations (Neher, 1971; Sakmann & Neher, 1984; Stuart & Sakmann, 1995; Angelo et al., 2007; Bar-Yehuda et al., 2008). The extracellular recordings in vivo using metal microelectrodes arrays (MEA) constitute the second and the earliest approach, dating from the works of Emil Heinrich du Bois-Reymonds who introduced the first non-polarizable electrodes and high-sensitivity multipliers in the middle of the 19th century (Pearce, 2001). Extracellular recordings via intracranial windows in experimental animals and human patients are today a daily practice in many institutes around the world (Brinkmann et al., 2009; Gnatkovsky et al., 2008; Wilent et al., 2011). In more modern times, this technique has been divided into two fields of study, one dedicated to the understanding of the postsynaptic potentials (i.e. the local field potential, LFP) (Buzsáki, 2006) and the other to the genesis of the neuronal spiking [i.e. the multi(single) unit activity, M(S)UA] (Stark & Abeles, 2007; Wilson, 2010).

The development of biophysical models, with the particulars for each technique, to explain the data has been an important issue in the history of both experimental approaches. The existence of incompatible specificities, together with the spontaneous segregation of the electrophysiologists into two independent research communities, has gradually created a gap between the theoretical frameworks underlying these approaches. The clearest one is the assumption of an extracellular space having a resistance negligible with respect to the resistance of the intracellular space when creating models for individual neurons from whole-cell voltage/current clamp data (Rall, 1957; 1959; 1960; 1964). Perhaps, this assumption originated from the fact that the intracellular space along dendritic branches always contains long and narrow domains, which give them a very large effective resistance compared to that of the extracellular space. Quite the opposite, the volume fraction of the extracellular and intracellular spaces is about 0.3 in most tissue preparations (Lehmenkühler et al., 1993), a fact that makes the extracellular resistance to be in the extreme case 1.3 times higher than that of the intracellular

(Appendix-1). From an experimental perspective, whole-cell voltage/current clamp are the result of observing either induced voltage differences or current flows between a glass-microelectrode, whose tip is inside some intracellular domain, and a far-away bath electrode. In contrast, extracellular recordings capture voltage differences in the extracellular space from metal microelectrodes that are in close proximity to the neurons. With the development of silicon-based technologies and the micro-electro-mechanic systems "MEMS", MEAs are built everyday with more precision, which has triggered remarkable advances in modeling and data analysis. Performing current source density (CSD) analyses based on both models of cortical columns and the Poisson equation for the electric potentials constitutes one of the most standard techniques used nowadays to analyze the LFPs (Somogyvári et al., 2005; Pettersen et al., 2006; Lindén et al., 2010; Gaute & Einevoll, 2010). Similarly, methods employed to detect and classify neuronal spiking are progressively founded on biophysical models of single neurons acting in a highly conductive medium.

In modern times, several groups have established techniques to perform whole-cell current clamp recordings (or juxtacellular recordings) (Joshi & Hawken, 2006; Pinault, 2008) in vivo. In more ambitious projects, these recordings have been observed simultaneously with LFPs and M(S)UA from MEA either in situ (Gloveli et al., 2005) or in vivo (Harris et al., 2000; Henze et al., 2000) situations. While each theoretical framework referred above has been always consistent with the respective experimental approach, they have to be carefully used to explain such type of concurrent data. The classical way to link intracellular and extracellular recording modalities, from a modeling viewpoint, is by solving the respective forward generative problems in a sequential strategy. In the first step of this strategy, multi-compartmental models, useful to describe the membrane potentials, are created with the particularities of each neuron. In a second step, primary and returning current sources across the entire membranes of the neurons are calculated using these models. The validity of such a source model lies beneath the assumption of a space-shunted extracellular space. Finally, the Poisson equation is used to calculate the distributions of electric potentials in the extracellular space created by the trans-membrane monopolar sources (Gold et al., 2006). The major contradiction in this strategy is the fact that the first step is performed under the assumption of a zero extracellular resistance while the last one is, by principle, based on the existence of an extracellular electric conductivity field (Goto et al.,

2010). This strategy might be valid and useful in situations where the electrodes utilized to record the extracellular potentials are far away from the neuronal populations. However, in our opinion when these electrodes are immersed inside the neuronal populations, and are hence in very close proximity to the neurons generating the extracellular potentials, other theoretical frameworks may be more appropriate. Riera et al. (2006) proposed a multi-compartmental model for the pyramidal cells in the human visual cortex, which explicitly incorporates extracellular resistances at all compartments. The interactions between compartments were only electrotonic (no active ionic conductances) in this preliminary work and merely three representative compartments were considered to describe the soma as well as the apical-tuft and basal dendrites. The voltage differences along the extracellular resistances were used by these authors to models mesoscopic dipolar sources underlying the EEG recordings.

In this paper, we created a new theoretical formalism to construct biophysical models for neurons which has been inspirited in the conceptual framework proposed by Riera et al. (2006). This formalism is based on four constitutive electric devices for most of the typical cellular structures: the collector (soma), the propagator (trunk), the integrator (dendritic branches) and the 3D-connector (dendritic bifurcations). The innovative aspect in these devices is the inclusion of multiple extracellular resistances that adequately can be used to absorb the geometrical aspects of each cellular structure. First, we created the theoretical equations and provided instructions on how to use the four devices to create neurons with dissimilar morphologies. Second, we developed the particulars for the layer 5 tufted pyramidal cells (PCL5). In order to study the effect of the extracellular resistances in the pyramidal cells on the action potential (AP) back-propagation, we surveyed literature on the kinetics and permeability profiles of the most important ionic channels in this particular cell type. Our model was able to accommodate experimental data about the amplitude decay and peak delay of back-propagating APs more precise than the same model when all extracellular resistances were set to zero. We defined in a direct way the extracellular potentials near a particular neuron as voltage drops in the extracellular resistances. We used such a construct to create individual CSDs for back-propagating APs and discussed our results together with experimental data reported in the literature (Bereshpolova et al., 2007). We could estimate close-field monopolar, dipolar and quadrupolar contributions to the CSD by a single pyramidal cell. We concluded that,

even for models based on the Kirchhoff's laws for circuit loops, monopolar and quadripolar sources emerge in the CSD analysis as a result of the mismatch between the physical assumptions made to solve the forward problems in these two tissue substrates, i.e. on one hand we assumed the electric fields were quasistatic (Poisson equation), and on the other hand we introduced highly dispersive elements (membrane capacitances). Finally, we extended our model of the pyramidal cells to include elemental current sources in parallel to the extracellular resistances for each compartment, which was very useful to mimic current stimulation by microelectrodes in close proximity to the neurons. Using this last model, we were able to evaluate the sensitivity of the PCL5 to the different stimulation locations along the cellular trunk.

Materials and methods

A general framework for modeling neuronal activity

In the proposed theoretical formalism, neurons can be approximated by complex arrays of four elemental building blocks (Figure 1-A2 and B2), which are endowed with ionic channels. These building blocks, which are named the integrator (dendritic branches), propagator (dendritic trunks), 3D-connector (branch bifurcation points) and collector (somas), contain detailed information about neuron geometries in terms of the particular values of intracellular, extracellular and membrane electrotonic parameters (i.e. resistances and capacitances). For instance, the pyramidal neurons (Figure 1-A1) are approximated by a collecting-soma attached on one side to the basal integrating dendrites and on the other to a long propagating trunk (Figure 1-A2). The trunk ends on a bulk of apical integrating dendrites. We can also attach oblique integrating dendrites to the trunk by means of a 3D connector. However, the spiny stellate neurons (Figure 1-B1) can be created by connecting integrators and a single collector in a spherical array (Figure 1-B2).

As shown in Figure 1-A2 and B2, the integrator is defined as a device which contains two parts: the first part possesses many dendritic branches with heterogeneous impedances and it receives synaptic inputs, and the second part produces a single output voltage at the last compartment of the integrator which is used as an input in any other building block connected to it. The propagator refers to a device that propagates inputs over long distances separating two building

blocks. The propagator is composed of several compartments which can be non-uniform. By means of a 3D-connector, we can create links between three particular building blocks that simulate the points of electrotonic division (e.g. dendritic bifurcations). The collector represents a device that collects the outputs from specific arrays of building blocks and generates from them the final spiking state of the cell.

The extracellular space (ECS) is composed of the cerebral spinal fluid that distributes along the narrow interstitial space between the neuronal processes. Nowadays, it is well established that the ECS occupies a volume fraction of between 15% and 30% in normal adult brain tissue (Sykova & Nicholson, 2008). For general cases, the equivalent electrical circuits of the building blocks in the frequency domain are shown in Figure 2-A, B, C, and D for the integrator, propagator, 3D-connector, and collector, respectively. Every equivalent electrical circuit contains the resistance of both the intracellular space (ICS) and the ECS, as well as the membrane complex resistance. By using the Kirchhoff's laws for these circuits, we were able to obtain theoretical formulas for the changes in the membrane potentials for each building block (Appendix-2).

An application: AP back-propagation in PCL5

The morphological properties

As an example, we will apply this model to study back-propagating APs in PCL5 (Figure 1-A1). In this model, the PCL5 is composed of three interconnected building blocks (Figure 3, left) embedded with ionic channels: integrator, propagator, and collector.

For the case of stimulating a PCL5 through the injection of intracellular currents in the soma, the ionic channels rather than the synapses play a key role for back-propagating APs. Here, the oblique and basal dendrites were ignored. Therefore, this simple model of PCL5 contains an integrator with only one apical-tuft branch, a propagator with 10 compartments, and a collector with only one input coming from the propagator. However, the morphology of PCL5 can be non-uniform within compartments. For a precise result, we assumed that all compartments of the propagator can be divided into two equal parts in the electrical circuit (Figure 2-B): the upper and lower part. Note that the distal apical integrating dendrite is connected to the first compartment of the propagator and

the collecting soma is connected to the last compartment of the propagator. The entire model of AP back-propagation inside the PCL5 was programmed in MATLAB (i.e. this code is available by request).

In our model, we assumed that the volume of the ECS in close proximity to the PCL5 was equal to 30% of the volume of its ICS, which determine the upper bound for the extracellular resistance. We used geometrical parameters to calculate the membrane resistances, and the resistance of the ICS and the ECS for every compartment of the integrator, the propagator and the collector in our model. The calculation of those resistances is shown in the Appendix-1.

To estimate the geometrical properties (length, diameter, area, volume) of PCL5s, we performed whole-cell somatic patch-clamp experiments using somatosensory coronal slices (300 μm) of young Wistar rats (P14-P16). The artificial cerebral spinal fluid solution contained (in mM): 125 NaCl, 25 $NaHCO_3$, 25 glucose, 2.5 KCl, 1.25 $NaH_2PO_4H_2O$, $2CaCl_22H_2O$ and 1 $MgCl_26H_2O$. Recording electrodes (5–7.5 MΩ) were loaded with intracellular solution contained in (mM) 115 potassium gluconate, 20 KCl, 2 Mg-ATP, 2 Na2-ATP, 10 sodium phosphocreatine, 0.3 GTP, 10 HEPES, 0.05 Alexa fluor hydrizide 594. Sixteen cells were selected based on their firing patterns (regular spiking) and their image stacks recorded by the Two Photon Laser Scanning Microscopy were combined using a volume integration and alignment system (VIAS) (Rodriguez et al., 2003). Geometrical properties of selected PCL5 were evaluated using the Neuron Studio software (Rodriguez et al., 2003): (1) As for the single branch of the integrator, its morphological properties were obtained from averaged data of three branches. The last compartment of the integrator which connects the propagator and integrator was approximated as a cylinder and its length and diameter measured; (2) The propagator was assumed as a cylinder and divided into 10 compartments (Figure 3, right A) whose lengths and diameter were determined (Figure 3, right B1). The collector was subjectively classified into three formats according to their different shapes (i.e. triangular, round and oval, Romand et al., 2011). Thus, collectors were approximated by a sphere whose diameters were measured (Figure 3, right B2). All animal procedures were reviewed and approved by the Tohoku University Animal Studies Committee.

The resistance of membranes, ICS and ECS belonging to each of the building blocks are evaluated base upon the mean values of lengths and diameters gathered

from sixteen PCsL5 (Table 1).

The voltage-gated ionic currents

Three voltage-gated ionic channels are embedded in this model: sodium (Na), potassium fast (K_f), and potassium slow (K_s). The voltage-gates of these three ionic conductances were based on nucleated patched recordings from PCsL5 (Korngreen and Sakmann, 2000). All the conductances were modeled using Hodgkin-Huxley type of models (Hodgkin and Huxley, 1952).

The kinetic equations were defined as follow (Keren et al., 2005):

1. Sodium

$$g_{Na} = \bar{g}_{Na} m^3 h$$

Activation: $m_\infty = \dfrac{1}{1+e^{-\frac{V_m+38}{10}}}$ $\tau_m = 0.058 + 0.114 e^{-(\frac{V_m+36}{28})^2}$

Inactivation: $h_\infty = \dfrac{1}{1+e^{\frac{V_m+66}{6}}}$ $\tau_h = 0.28 + 16.7 e^{-(\frac{V_m+60}{25})^2}$

2. Potassium fast

$$g_{Kf} = \bar{g}_{Kf} a^4 b$$

Activation: $a_\infty = \dfrac{1}{1+e^{-\frac{V_m+47}{29}}}$ $\tau_a = 0.34 + 0.92 e^{-(\frac{V_m+71}{59})^2}$

Inactivation: $b_\infty = \dfrac{1}{1+e^{\frac{V_m+66}{10}}}$ $\tau_b = 8 + 49 e^{-(\frac{V_m+73}{23})^2}$

3. Potassium slow

$$g_{Ks} = \bar{g}_{Ks} \gamma^2 (0.5 s_1 + 0.5 s_2)$$

Activation: $\gamma_\infty = \dfrac{\alpha_\gamma}{\alpha_\gamma + \beta_\gamma}$ $\tau_\gamma = \dfrac{1}{\alpha_\gamma + \beta_\gamma}$

$$\alpha_\gamma = \frac{0.0052(V_m - 11.1)}{1 - e^{-\frac{V_m - 11.1}{13.1}}} \qquad \beta_\gamma = 0.02e^{-\frac{V_m + 1.27}{71}} - 0.005$$

Inactivation: $s_{1,\infty} = s_{2,\infty} = \frac{1}{1 + e^{\frac{V_m + 58}{11}}}$

$$\tau_{s1} = 360 + [1010 + 23.7(V_m + 54)]e^{-(\frac{V_m + 75}{48})^2}$$

$$\tau_{s2} = 2350 + 1380e^{-0.011V_m} - 210e^{-0.03V_m}$$

The conductance profile of each of these three channels along the trunk of the PCL5 was based on data provided by Rhodes (2006). Since those data were obtained from 40 days/old Wister rats, the same profiles were kept, but scaled by a factor of 0.3 to properly reproduce them as reported for juvenile rats (P14-P16), the conductance profile of (Na) sodium (Stuart & Sakmann, 1994) and (K_f & K_s) potassium (Schaefer et al., 2007) channels.

The extracellular current sources generated by PCL5

In contrast to previous studies, here we approximated the extracellular electric potentials at any position very close to the PCL5 by the voltage drop in the respective extracellular resistance at each compartment. In such an approach, the contributions to the LFP of the trans-membrane current sources of other compartments are neglected. This hypothesis is needed to simplify the theoretical analysis. In our case, the extracellular resistance constitutes an important element of the neuronal circuit as it has an impact on the final dynamics of the membrane potential. We used this framework to simulate the LFP from our PCL5 model. All LFP signals were referenced to a single reference electrode which was near the distal trunk in the extracellular space, other electrodes were in correspondence to the resistance of the ECS (Figure 4-A). In the Figure 4, R_i^e shows the *i* th resistance of the ECS which is in between the *i* th and *i+1* th compartment, U_i shows the voltage of R_i^e. The details of the electric circuit are shown in Figure 4-B.

The LFPs were calculated by the following equations (Appendix 3):

$$V_i = \sum_{k=1}^{i} U_k$$

Note that while calculating the LFP.the summation by the index *k* has to be

performed through all extracellular resistances of interest. To analyze the distribution of diminutive electric sources $s = -\sigma\nabla^2\varphi$ produced by a particular neuron inside a mesoscopic region (i.e. a cortical column) from simulated LFPs $\varphi(\vec{r}_i) = V_i$, $i = \{1, \cdots, N\}$, at discrete recording sites $\vec{r}_i$ along the cortical lamina, we used the iCSD method (Pettersen et al., 2006; **iCSDplotter** software, version 0.1.1). The parameters used in this analysis were: **a)** the disk diameter *d* for the sources, which was 0.5 *mm*, **b)** the standard deviation for the Gaussian filter, which was 50 *μm*, and **c)** the electric conductivity σ (homogenous media), which was 3 *mS/cm* (Goto et al., 2010). The thickness *l* of the cortical columns was 2 *mm*. Assuming the cortical columns were perfect cylinders, their volumes $V = \pi(d/2)^2 l$ would be 0.39 mm^3. We did not use boundary conditions (i.e. free electric potentials). The mathematical definition of monopoles *m(t)*, dipoles *d(t)*, and quadrupoles *Q(t)* from the volume sources *s* are given by the following equations (Riera et al., 2011):

$$m_z(t) = \pi\left(\frac{d}{2}\right)^2 \int_0^l s(z,t)dz$$

$$d_z(t) = \pi\left(\frac{d}{2}\right)^2 \int_0^l s(z,t)(z - z_m)dz$$

$$Q_z(t) = \pi\left(\frac{d}{2}\right)^2 \int_0^l s(z,t)(z - z_m)^2 dz$$

The vector $\vec{r}_m$ indicates the center of gravity of the cortical column, and the value z_m stands for its respective laminar coordinate. The axis *z* is defined in the direction perpendicular to the neocortex with positive and negative values toward the supragranular and infragranular layers, respectively.

Stimulating the PCL5 by extracellular current injection

Due to the existence of a resistance of the ECS, we also were able to inject electric currents to the ECS to induce spiking in PCL5. In Figure 5, we show the original electric circuit which contains the resistance of the ECS (Figure 5-A) and the modified electric circuit to account for an extracellular current injection (Figure 5-B and C). In our model, an injection of an electric current in the ECS close to a compartment of the neuron can be represented by an external current source in

parallel to the extracellular resistance of that compartment (Figure 5-B). By means of Norton's theorem, we can transform this parallel circuit into a serial circuit with an equivalent voltage source (Figure 5-C). Hence, we can directly add the voltage injection source to the equivalent electrical circuits of the building blocks in our multi-compartmental model.

The equivalent equation is as follows:

$$E_i^{inje} = I_i^{inje} \cdot R_i^e$$

By using Kirchhoff's laws for these circuits, we can include these serial voltage sources in the original equivalent equations of the building blocks of the multi-compartmental model (Appendix-2).

Results

Intracellular stimulation of PCL5

Figure 6 shows the propagation of an AP train from the soma to the distal trunk with both cases: a zero and a nonzero resistance for the ECS. The membrane potential was held at -70 mV and a square pulse current of 200 pA injected at the soma for 150 ms. In both cases, the peak amplitude of APs remains constant after a very short transitory period. There is a good concord between these results and those provided in a previous experiment (Chang & Luebke, 2007). From these simulations, it can be noticed that amplitude of back-propagating APs is not affected by the resistance of ECS. On the contrary, number of spikes is slightly reduced when Re is not zero. As a consequence of the uncertainty in determining current leakages in whole-cell voltage clamp experiments and the variability in the cell dimensions, the number of spikes does not constitute a suitable experimental criterion to precisely evaluate the impact of extracellular resistance in the cellular signaling. A more meticulous evaluation can be achieved by inspecting the shape of the back-propagating APs.

We compared two single APs from these simulated data with equivalent initiation times (Figure 7). In order to quantify the differences of these two single APs, we used the amplitude decay and peak delay curves of the back-propagating APs (Figure 8). First, we chose the data of three previous studies reporting the APs decay and delay curves in PCL5 (i.e. Stuart & Sakmann, 1994; Gulledge & Stuart,

2003; Bar-Yehuda et al., 2008; data summarized in Figure 8-A). Second, in those common sites along the PCL5 trunk we averaged the decay and delay values reported in these previous studies. Finally, we compared the mean experimental curves with those obtained from our simulated back-propagating APs. The decay curves were similar in these previous studies. However, there were significant differences among these three studies in the estimated delays curves, i.e. about 2 ms discrepancy at the distal apical dendrites.

We compared the decay and delay information calculated from the back-propagating APs in our simulations with those obtained from averaging previous experimental data (Figure 8-B). We could not find an obvious difference in simulated amplitude-decays for the cases of zero and nonzero resistance of the ECS. The predictions in both cases were very similar to that mean amplitude-decay curve experimentally estimated (Figure 8-B, left). The estimation errors were slightly smaller for the case of nonzero resistance of the ECS (i.e. 4.56) compared to the case of zero resistance of the ECS (i.e. 4.92). Taking into consideration that we performed this simulations using the upper bound for the resistance of the ECS, we concluded that the existence of ECS resistance will never affect the amplitude-decay curve of back-propagating APs in the PCL5. However, we found that in the case of having a zero resistance of the ECS the APs propagate faster along the PCL5 trunk back to the apical dendrites (Figure 8-B, right), as quantified through the peak-delay curve. By comparing the simulated peak-delay curves with that mean curve experimentally estimated, we concluded that the estimation errors were significant larger in the case of having the ECS voltage-space clamped (i.e. 0.68) compared to the case of a highly resistive ECS (i.e. 0.37). However, further experiments are required to verify this conclusion since the aforementioned discrepancies in the experimentally estimated peak-delay curves, in spite of having used equivalent species (Wistar rats), brain regions (neocortex) and animal ages.

Using the strategy proposed in the material and methods, we simulated the LFP and calculated the respective CSD for the case of having an ECS with a nonzero resistance. In this particular case, for the cell to fire a single AP a current of 200 pA was injected for 5 ms (Figure 9). The calculated CSD spatiotemporal pattern was very close to that estimated from experimental data (Bereshpolova et al., 2007). Based on our calculated CSD, we determined the multipolar components generated by a single PCL5 while APs are back-propagating along its trunk. Note that our estimators are only valid if the microelectrodes are in close proximity to

the PCL5, e.g. a linear probe with electrodes arranged parallel to the PCL5 at a distance < 50 μm from it. In contrast to the results obtained by Milstein & Koch (2008), we were able to distinguish monopolar and quadrupolar contributions to the LFP which were comparable in size to that of the dipolar source model. The strategy in Milstein & Koch (2008) was to solve the discrete cable equation assuming a zero resistance of the ECS and use the resulting trans-membrane currents (i.e. both primary and returning currents) to calculate the LFP through the Poisson equation. Therefore, their results originated from both the local dipolar character of the trans-membrane current sources and the instantaneous propagation of the electric field in pure resistive media (i.e. the quasistatic approach). In our case, the strategy used to calculate the LFP takes into account the dynamic changes in the extracellular potentials which are caused by the existence of polarization effects along the cellular membranes.

Extracellular stimulation

We used the proposed strategy to stimulate the PCL5 using extracellular current injection at the level of each compartment. We applied extracellular electric currents (i.e. square pulses: 50 ms – 250 ms) at different positions of the PCL5 to generate a train of APs in its soma. The amplitudes of the electric currents were adjusted to reproduce trains of AP with similar spike frequency/rate. Figure 10 illustrates such a procedure for four particular positions (i.e. the soma, and a site in the proximal, middle and distal trunk).

In Figure 11, we showed the relationship between the amplitudes of the injected electric current into the ECS and the distance from the soma. We found that the farer we are from the soma the higher the current have to be injected to equivalently stimulate the PCL5, and that it follow a exponential-like relationship. The estimated sensibility profile of the PCL5 to extracellular current injection will allow us to create in the near future strategies to selectively stimulate this particular cell type from specially designed MEAs.

Discussion

For establishing neuronal model for any types of neurons, we created a new theoretical formalism which contains the resistance of ECS. Comparing the number of APs in the "R_e is not zero" study and the "R_e is zero" study in the intracellular

stimulation results, we have shown that the APs could be generated more without the resistance of ECS. The result of decay showed that the resistance of extracellular space cannot affect the amplitude of neuronal APs in an obvious way. However, we could find an obvious difference of spread speed of APs from soma to distal trunk in delay result. We also created a new method for LFP and CSD simulation, these simulation results showed that our model can provide simulation data which was very close to the experimental data, and based on our CSD data, the monopoles, dipoles and quadrupoles results could be calculated precisely. Since our model included the ECS, we were able to stimulate neuron at ECS and evaluate the sensitivity of the neuron to the stimulation location along the cellular trunk. We showed the nonlinear relationship between the amplitude of the injected current in the ECS and the injected distance from soma in the extracellular stimulation results, we found that we needed more injected current to generate neuronal APs in the extracellular space. Based on the safe region for injection current in the ECS during the experiment, we were able to find the limit position which could inject the current up to 2μA.

Riera et al. (2006) represented the electrotonic propagation of the membrane potentials in the PCL5 of the human visual cortex using a three-compartment model that included the apical dendrites, basal dendrites and the soma. These authors used such a model to estimate crucial physiological parameters in the cortical microcircuit from large-scale EEG data which were obtained from healthy subjects undergoing a flickering checkerboard visual stimulation paradigm (Riera et al., 2007). In then current study, we extended this previous model not only to include active ionic currents, but also to represent cells with other morphologies through the combination of four basic electrotonic devices: the integrator, the propagator, the 3D-connector and the collector. Each of these devices, which in principle could comprise multiple compartments, is able to connect to any other device by means of terminals (open circuits) having free voltage differences as the linking physical magnitudes. As in Riera et al. (2006), the extracellular electric potential was defined as the voltage drops in the resistances of the extracellular space for each compartment. Additionally, we obtained mathematical formulas for the case in which sources of electric currents were in parallel to the extracellular resistances. The last theoretical result allowed us to create a realistic profile of PCL5 sensitivity to external current stimulation by means of MEAs in close proximity to the cells, a subject of relevance in developing brain machine interfaces.

We provided a link between the intracellular (membrane potentials) and extracellular (LFP/MU(S)A) recordings without assumptions of both a charge balance along the cellular membrane and a quasistatic approach for the electric field. However, our theoretical model is only valid for recording sites in close proximity to the neurons of interest. We were able to reproduce similar spatiotemporal patterns in the extracellular CSD generated by back-propagating APs, such as those reported by Bereshpolova et al. (2007). Our model was also able to reproduce experimentally observed curves for the amplitude decay and peak delay of back-propagating APs.

The decay/delay for back-propagating APs: The discrepancies

To evaluate the impact of introducing an extracellular resistance in the multi-compartmental models of PCL5, in this study we used the decay and delay curves of back-propagating APs in these particular cell types obtained by different laboratories (Stuart & Sakmann, 1994; Gulledge & Stuart, 2003; Bar-Yehuda et al., 2008). The first report dates from the early 90's (Stuart & Sakmann, 1994). These authors performed patch-clamp recordings from dendrites of neocortical pyramidal cells using parasagittal neocortical brain slices from 2-week-old Wistar rats. Almost ten years later, Gulledge & Stuart (2003) obtained similar measurements from coronal brain slices containing the prelimbic prefrontal cortex from 3- to 5-week-old Wistar rats. In Stuart & Sakmann (1994)'s study, the decay curve was similar to that reported by Gulledge & Stuart (2003), but the delays were much larger, i.e. the APs reached a site about 500 μm from the soma 2 ms slower than in Gulledge & Stuart (2003). Using sagittal slices from 5- to 7-week-old Wistar rats, more recently Bar-Yehuda et al. (2008) reported similar decay/delay curves to those found by Gulledge & Stuart (2003). We realized that there is a discrepancy in the delay curve reported in the initial works by Stuart & Sakmann (1994) and in those obtained in more contemporary studies (Gulledge & Stuart, 2003; Bar-Yehuda et al., 2008). These three studies all used Wistar rats. We opted to use averaged data from these three studies for both decay and delay curves. We believe further studies are required to verify whether these curves depend on either age, specie, brain region, or PCL5 subtype. Currently, we believe that the average data has the most valid curves possible.

As is shown in Figure 8, a multi-compartment model for PCL5 that includes extracellular resistances different from zero generates APs propagating more

slowly toward the apical tuft. To explain this phenomenon, we use a simplified model of a membrane circuit (one single compartment) that includes not only membrane and intracellular resistances, but also a nonzero extracellular resistance. The membrane potential can be calculated by the equation:

$$C\frac{dV}{dt} = -\frac{1}{R^*}V + I_{ext}$$

In this equation, R^* is an equivalent resistance that results from having a membrane resistance in parallel to a series of intracellular R_i and extracellular R_e resistances. The time constant for the circuit will be $\tau = R^*C$. Therefore,

$$\frac{1}{R^*} = \frac{1}{R_m} + \frac{1}{R_{ei}} = \frac{R_m + R_{ei}}{R_m R_{ei}}$$

Where $R_{ei} = R_e + R_i$.

As we mentioned earlier, $R_e = 1.3R_i$. We compared the R^* in both cases: "R_e is not zero" and "R_e is zero".

$$\frac{1}{R^*_{R_e \neq 0}} = \frac{R_m + R_{ei}}{R_m R_{ei}} = \frac{R_m + 2.3R_i}{2.3R_i R_m}$$

$$\frac{1}{R^*_{R_e = 0}} = \frac{R_m + R_i}{R_m R_i} = \frac{R_m + R_i}{R_i R_m}$$

It can be easily demonstrated $\frac{R^*_{R_e \neq 0}}{R^*_{R_e = 0}} > 1$, which implies $\tau_{R_e \neq 0} > \tau_{R_e = 0}$.

An alternative explanation for the AP retardation in the case of nonzero extracellular resistive originates from a thermodynamic viewpoint. For electrical circuits with more resistive elements, which are dissipative, the net production of heat in a given time window $Q = IRt$ will be higher. Such an energy transformation process could underlie both larger delays in the propagation of APs.

The charge-balanced hypothesis: The extracellular potential models

From a classical approach, the connection between intracellular and

extracellular recordings is based on assuming the existence of microscopic current sources across the cellular membrane of the entire neurons. Therefore, the extracellular electric potentials are naturally calculated by using the Poisson equation for quasistatic electric fields. This strategy might be valid and useful in situations where the microelectrodes utilized to record the extracellular potentials are far away from the neuronal populations of interest. However, in situations where these microelectrodes are in close proximity to the neurons generating the extracellular potentials, such a classical approach may produce inaccurate results. On the other hand, such a source model implies a microscopic charge balance in the cellular membranes. Riera et al. (2011) provided recent evidence that refutes such a working hypothesis at the mesoscopic level. In the barrel cortex of Wistar rats undergoing a whisker stimulation protocol, these authors found important contributions from monopolar and quadrupolar current sources to the extracellular potentials at the mesoscopic level. The role of multipolar current sources in the genesis of LFP/MU(S)A has been evaluated in the past (Milstein & Koch, 2008), where dipolar components were suggested to be larger than other multipolar moments. Therefore, in order to clarify whether or not the dipolar moment is the only one contributing to the genesis of LFPs future evaluations are needed.

Poisson equation vs. Kirchhoff circuit laws

The major problem in previous strategies that attempted to link models for the intracellular and extracellular experimental approaches is the strong inconsistency in the underlying assumptions. On the one hand, researchers use the quasistatic approach for the electric field, which was initially introduced to describe the propagation of electric and magnetic fields inside the biological tissues (Plonsey & Heppner, 1967), to estimate the extracellular electric potential $\varphi(\vec{r})$ everywhere from known microscopic current sources s across the membrane of the neurons. For the electric field, this approach results in the well-known Poisson equation $\nabla\cdot(\sigma\nabla\varphi)=-s$. In the frequency range of observing electrophysiological phenomena ($\omega \ll 100\,kHz$), dispersive effects in the tissues are ignored (i.e. pure resistive media). Under such a condition, the conductivity σ reflects mostly the macroscopic conductivity which is determined by the characteristics of the cell suspension (i.e. volume fraction of the extracellular and intracellular spaces) and does not include any contribution originating from the existence of a highly dispersive membrane. Nowadays, we are familiar with the fact that such an approach is not valid even for the lowest frequency range ($\omega \ll 100\,Hz$) of the LFP (Gabriel et al., 1996a,1996b,

1996c, 2009; Bédard & Destexhe, 2009; Bédard et al., 2010). On the other hand, the differential equations used to describe the membrane potentials in neurons, by nature, originate from the fact that there is a capacitor separating the intracellular and the extracellular spaces. In such differential equations, the actual brain sources across the cellular membranes are incorporated following Kirchhoff's circuit laws. As demonstrated in this paper, we have to be careful when representing these actual current sources at a mesoscopic level with equivalent dipolar models that neglect the contribution of monopolar and high-order multipolar moments to the LFPs (Riera et al., 2011).

Acknowledgements

First, I would like to appreciate KAWASHIMA Lab NMD group to support me to do my master research, I thank Dr. Hervé and Dr. Takakuni to help to do so many experiments, and I especially really acknowledge Prof. KAWASHIMA and Associate Prof. REIRA gave me so many advices to help finish my master paper. I also would like to thank Prof. Juan Carlos Jimenez from the Institute of Cybernetics and Mathematics Applied to Physics for helping us to create suitable MATLAB code for integrating large stochastic differential equations. This work has been supported by the following grants: a) Japan-Canada Joint Health Research Program (JSPS) "The neuroarchitectonic determinants of EEG recordings"; b) Grant-in-Aid for Scientific Research (B) 23300149; c) JSPS Grant-in-Aid for Young Scientists (B) 23700492

References

Angelo K., London M., Christensen SR., & Häusser M. (2007). Local and global effects of I(h) distribution in dendrites of mammalian neurons. J Neurosci. 27(32):8643-53.

Bar-Yehuda D., Ben-Porat H., & Korngreen A. (2008). Dendritic excitability during increased synaptic activity in rat neocortical L5 pyramidal neurons. Eur J Neurosci. 28(11):2183-94.

Bédard C., & Destexhe A. (2009). Macroscopic models of local field potentials and the apparent 1/f noise in brain activity. Biophys J. 96(7):2589-603.

Bédard C., Rodrigues S., Roy N., Contreras D., & Destexhe A. (2010). Evidence for frequency-dependent extracellular impedance from the transfer function between extracellular and intracellular potentials: intracellular-LFP transfer function. J Comput Neurosci. 29(3):389-403.

Bereshpolova Y., Amitai Y., Gusev AG., Stoelzel CR., & Swadlow HA. (2007). Dendritic backpropagation and the state of the awake neocortex. J Neurosci. 27(35):9392-9.

Brinkmann BH., Bower Mr., Stengel KA., Worrell GA., & Stead M. (2009). Large-scale electrophysiology: acquisition, compression, encryption, and storage of big data. J Neurosci Methods. 180(1):185-92.

Buzsáki G. (2006). Rhythms of the Brain. New York: Oxford Univ. Press. p.89–92.

Chang YM., & Luebke JI. (2007). Electrophysiological diversity of layer 5 pyramidal cells in the prefrontal cortex of the rhesus monkey: in vitro slice studies. J Neurophysiol. 98(5):2622-32.

da Costa NM., & Martin KA. (2011). How thalamus connects to spiny stellate cells in the cat's visual cortex. J Neurosci. 31(8):2925-37.

Einevoll GT. (2010). Modeling of extracellular potentials recorded with multicontact microelectrodes. 7th Int. Meeting on Substrate-Integrated Microelectrodes.

Gabriel C., Gabriel S., & Corthout E. (1996). The dielectric properties of biological tissues: I. Literature survey. Phys Med Biol. 41(11):2231-49.

Gabriel C., Peyman A, & Grant EH. (2009). Electrical conductivity of tissue at frequencies below 1 MHz. Phys Med Biol. 54(16):4863-78.

Gabriel S., Lau RW., & Gabriel C. (1996). The dielectric properties of biological tissues: II. Measurements in the frequency range 10 Hz to 20 GHz. Phys Med Biol. 141(11):2251-69.

Gabriel S., Lau RW., & Gabriel C. (1996). The dielectric properties of biological tissues: III. Parametric models for the dielectric spectrum of tissues. Phys Med Biol. 41(11):2271-93.

Gloveli T, Dugladze T, Rotstein HG, Traub RD, Monyer H, Heinemann U, Whittington MA, & Kopell NJ. (2005). Orthogonal arrangement of rhythm-generating microcircuits in the hippocampus. Proc Natl Acad Sci U S A. 102(37):13295-300. Epub 2005 Sep 2.

Gnatkovsky V., Librizzi L., Trombin F., & de Curtis M. (2008). Fast activity at seizure onset is mediated by inhibitory circuits in the entorhinal cortex in vitro. Ann Neurol. 64(6):674-86.

Gold C., Henze DA., Koch C., & Buzsáki G. (2006). On the Origin of the Extracellular Action Potential Waveform: A Modeling Study. J Neurophysiol. 95(5):3113-28.

Gold C., Henze DA., & Koch C. (2007). Using extracellular action potential recordings to constrain compartmental models. J Comput Neurosci. 23(1):39-58.

Goto T., Hatanaka R., Ogawa T., Sumiyoshi A., Riera J., & Kawashima R. (2010). An evaluation of the conductivity profile in the somatosensory barrel cortex of Wistar rats., J Neurophysiol. 104(6):3388-412.

Gulledge AT., & Stuart GJ. (2003). Action potential initiation and propagation in layer 5 pyramidal neurons of the rat prefrontal cortex: absence of dopamine modulation. J Neurosci. 23(36):11363-72.

Harris KD, Henze DA, Csicsvari J, Hirase H, & Buzsáki G. (2000). Accuracy of tetrode spike separation as determined by simultaneous intracellular and extracellular measurements. J Neurophysiol. 84(1):401-14.

Henze DA, Borhegyi Z, Csicsvari J, Mamiya A, Harris KD, & Buzsáki G. (2000). Intracellular features predicted by extracellular recordings in the hippocampus in vivo. J Neurophysiol. 84(1):390-400.

Hodgkin A., & Huxley A. (1952). A quantitative description of membrane current and its application to conduction and excitation in nerve. J. Physiol. 117:500–544.

Joshi S., & Hawken MJ., (2006). Loose-patch–juxtacellular recording in vivo—A method for functional characterization and labeling of neurons in macaque V1. Journal of Neuroscience Methods 156 (1-2):37-49.

Keren N., Peled N., & Korngreen A. (2005). Constraining compartmental models using multiple voltage recordings and genetic algorithms. J Neurophysiol. 94(6):3730-42.

Korngreen A., & Sakmann B. (2000) Voltage-gated K+ channels in layer 5 neocortical pyramidal neurones from young rats: subtypes and gradients. J Physiol. 525 Pt 3:621-39.

Larkman AU. (1991). Dendritic morphology of pyramidal neurones of the visual cortex of the rat: I. Branching patterns. J Comp Neurol. 306(2):307-19.

Larkman AU. (1991). Dendritic morphology of pyramidal neurones of the visual cortex of the rat: II. Branching patterns. J Comp Neurol. 306(2):320-31.

Larkman AU. (1991). Dendritic morphology of pyramidal neurones of the visual cortex of the rat: III. Branching patterns. J Comp Neurol. 306(2):332-43.

Lehmenkühler A., Syková E., Svoboda J., Zilles K., & Nicholson C. (1993). Extracellular space parameters in the rat neocortex and subcortical white matter during postnatal development determined by diffusion analysis. Neuroscience. 55(2):339-51.

Lindén H., Pettersen KH., & Einevoll GT. (2010). Intrinsic dendritic filtering gives low-pass power spectra of local field potentials. J Comput Neurosci. 29(3):423-44.

Milstein JN., & Koch C. (2008). Dynamic moment analysis of the extracellular electric field of a biologically realistic spiking neuron. Neural Comput. 20(8):2070-84.

Neher E. (1971). Two fast transient current components during voltage clamp on snail neurons. J Gen Physiol. 158(1):36-53.

Pearce JM. (2001). Emil Heinrich Du Bois-Reymond (1818-96). J Neurol Neurosurg Psychiatry. 71(5):620.

Pettersen KH., Devor A., Ulbert I., Dale AM., & Einevoll GT. (2006). Current-source density estimation based on inversion of electrostatic forward solution: effects of finite extent of neuronal activity and conductivity discontinuities. J Neurosci Methods. 154(1-2):116-33.

Pinault D. (2008). The Juxtacellular Recording-Labeling Technique. Vol. 54, Neuromethods, PP 41-75.

Plonsey R., & Heppner DB. (1967). Considerations of quasi-stationarity in electrophysiological systems. Bull Math Biophys. 29(4):657-64.

Rall W. (1957). Membrane time constant of motoneurons. Science 126: 454.

Rall W. (1959). Branching dendritic trees and motoneuron membrane resistivity. Exp. Neurol. 1: 491-527.

Rall W. (1960). Membrane potential transients and membrane time constant of motoneurons. Exp. Neurol. 2: 503-532.

Rall W. (1964). Theoretical significance of dendritic trees for neuronal input-output relations. In Neural Theory and Modeling, ed. R.F. Reiss. Stanford Univ. Press.

Rhodes P. (2006). The properties and implications of NMDA spikes in neocortical pyramidal cells. J Neurosci. 26(25):6704-15.

Riera J., Ogawa T., Goto T., Sumiyoshi A., Nonaka H., Evans A., Miyakawa H., & Kawashima R. (2011). Pitfalls in the dipolar model for the neocortical EEG sources. Journal of neurophysiology. (Revision).

Riera JJ., Wan X., Jimenez JC., & Kawashima R. (2006). Nonlinear local electrovascular coupling. I: A theoretical model. Hum Brain Mapp. 27(11):896-914.

Riera J., Jimenez JC., Wan X., Kawashima R., & Ozaki T. (2007). Nonlinear Local Electro-Vascular Coupling. Part II: From Data to Neural Masses. Human Brain Mapping, 28, 335-354.

Rodriguez A., Ehlenberger D., Kelliher K., Einstein M., Henderson SC., Morison JH., Hof PR., & Wearne SL. (2003). Automated reconstruction of three-dimensional neuronal morphology from laser scanning microscopy images. Methods 30:94-105.

Romand S., Wang Y., Toledo-Rodriguez M., & Markram H. (2011). Morphological development of thick-tufted layer V pyramidal cells in the rat somatosensory cortex. Front Neuroanat. 5:5.

Sakmann B., & Neher E. (1984). Patch clamp techniques for studying ionic channels in excitable membranes. Annu Rev Physiol. 46:455-72.

Schaefer AT., Helmstaedter M., Schmitt AC., Bar-Yehuda D., Almog M., Ben-Porat H., Sakmann B., & Korngreen A. (2007). Dendritic voltage-gated K+ conductance gradient in pyramidal neurons of neocortical layer 5B from rats. J. Physiol 579 (3):737-752.

Somogyvári Z., Zalányi L., Ulbert I., & Erdi P. (2005). Model-based source localization of extracellular action potentials. J Neurosci Methods. 147(2):126-37.

Stark E., & Abeles M. (2007). Predicting movement from multiunit activity. J Neurosci. 27(31):8387-94.

Stuart G., & Sakmann B. (1995). Amplification of EPSPs by axosomatic sodium channels in neocortical pyramidal neurons. Neuron. 15(5):1065-76.

Stuart GJ., & Sakmann B. (1994). Active propagation of somatic action potentials into neocortical pyramidal cell dendrites. Nature. 367(6458):69-72.

Syková E., & Nicholson C. (2008). Diffusion in brain extracellular space. Physiol Rev. 88(4):1277-340.

Wilent WB., Oh MY., Buetefisch C., Bailes JE., Cantella D., Angle C., & Whiting DM. (2011). Mapping of microstimulation evoked responses and unit activity patterns in the lateral hypothalamic area recorded in awake humans. J Neurosurg.

Wilson DA. (2010). Single-unit activity in piriform cortex during slow-wave state is shaped by recent odor experience. J Neurosci. 30(5):1760-5.

Appendices

1. Calculation of resistances

In every compartment, l is length, d is diameter, A is area, and V is volume. The parameters A and V of every compartment are calculated from the l and d values. The calculation of the membrane resistance (R_m) is given by the following equation:

$$R_m = \frac{r_m}{1.92 \times A}$$

Here, the membrane resistivity (r_m) is equal to 40000 ($\Omega \times cm^2$). The factor 1.92 is introduced to account for the dendritic spine areas (Rhodes et al., 2006).

The calculation of the resistance of the ICS (R_i) is given by the following equation:

$$R_i = \frac{r_i \times l}{A_i}$$

Here, the resistivity of the ICS (r_i) is equal to 166 ($\Omega \times cm$).

The calculation of the resistance of the ECS (R_e) is given by the following equations:

$$R_e = 1.3 \times R_i$$

Proof:

$$\frac{R_e}{R_i} = \frac{\frac{r_e \times l}{A_e}}{\frac{r_i \times l}{A_i}} = \frac{r_e}{r_i} \times \frac{A_i \times l}{A_e \times l} = \frac{r_e}{r_i} \times \frac{V_i}{V_e} = \frac{63}{166} \times \frac{1}{0.3} \doteq 1.3$$

Here, the resistivity of the ECS (r_e) is equal to 63 ($\Omega \times cm$). We used the fact that the extracellular/intracellular volume fraction is approximately 0.3.

2. Model of building blocks

The cell's membrane unit can be modeled as a RC circuit and a primary current source, all in parallel (Figure 12). R and C stand for the membrane resistance and capacitance. In the frequency domain, an equivalent complex resistance of the circuit is defined as $R^* = \frac{R}{1 + j\omega\tau}$, where $\tau = RC$ represents the membrane time constant.

A: Model of the integrator

The integrator (Figure 1-A2 and B2) represents a device that possesses many branches with heterogeneous impedances and that receives a huge amount of inputs and produces a single output (i.e. a voltage difference). The integrator is useful to represent dendritic branches. This output is used as input in another electrotonic device. According to actual morphometry of dendritic trees (Larkman, 1991a, 1991b, 1991c), the integrator might comprise intermediate and terminal branches. We consider a model of the integrator composed mainly by a set of intermediate branches.

In order to determine the dynamic equations for the membrane potentials in each branch of the integrator, as well as in its last compartment, we use the Kirchhoff's laws. The equivalent circuit for this electrotonic device is shown in Figure 2-A, and the following equations can be easily obtained:

$$-V_0 - R_T{}^{ei} I - R_T{}^{e} I_T^{inje} - R_{A_1}{}^{ei} I_{A_1} - R_{A_1}{}^{e} I_{A_1}^{inje} + V_{A_1} = 0 \qquad \text{(A:a1)}$$

$$-V_0 - R_T{}^{ei} I - R_T{}^{e} I_T^{inje} - R_{A_2}{}^{ei} I_{A_2} - R_{A_2}{}^{e} I_{A_2}^{inje} + V_{A_2} = 0 \qquad \text{(A:a2)}$$

. . . . .
. . . . .
. . . . .

$$-V_0 - R_T{}^{ei} I - R_T{}^{e} I_T^{inje} - R_{A_k}{}^{ei} I_{A_k} - R_{A_k}{}^{e} I_{A_k}^{inje} + V_{A_k} = 0 \qquad \text{(A:ak)}$$

. . . . .
. . . . .
. . . . .

$$-V_0 - R_T{}^{ei} I - R_T{}^{e} I_T^{inje} - R_{A_M}{}^{ei} I_{A_M} - R_{A_M}{}^{e} I_{A_M}^{inje} + V_{A_M} = 0 \qquad \text{(A:aM)}$$

$$I = \sum_{k=1}^{M} I_{A_k} \qquad \text{(A:aM+1)}$$

$$-V_0 + R_T{}^{*} I^O + E_T{}^{*} = 0 \qquad \text{(A:aM+2)}$$

$$-V_1 - R_T{}^{e} I_1^{e} - R_T{}^{e} I_T{}^{inje} - R_T{}^{i} I_1^{i} + R_T{}^{*} I^O + E_T{}^{*} = 0 \qquad \text{(A:aM+3)}$$

$$I = I^O + I_1^{e} = I^O + I_1^{i} = 0 \qquad \text{(A:aM+4)}$$

Where $R_{\chi}^{ei} = R_{\chi}^{e} + R_{\chi}^{i}$, $\chi = \{T, A_k\}$.

The supra indexes "*e*" and "*i*" hold for the extracellular and intracellular spaces. I_{A_k} stands for a current entering the k th branch of the integrator. $I_{A_k}^{inje}$ stands for an extracellular injection current at the extracellular resistance of the k th branch of the integrator. I_T^{inje} stands for an extracellular injection current at the extracellular resistance of the last compartment of the integrator.

The expression of current I is obtained by dividing each A:ak th equation by $R_{A_k}^{ei}$ and summing all of them as follows:

$$I = \frac{\sum_{k=1}^{M} \frac{V_{A_k}}{R_{A_k}^{ei}} - V_0 \sum_{k=1}^{M} \frac{1}{R_{A_k}^{ei}} - I_T^{inje} R_T^{e} \sum_{k=1}^{M} \frac{1}{R_{A_k}^{ei}} - \sum_{k=1}^{M} \frac{I_{A_k}^{inje} R_{A_k}^{e}}{R_{A_k}^{ei}}}{1 + \sum_{k=1}^{M} \frac{R_T^{ei}}{R_{A_k}^{ei}}} \qquad \text{(A:b1)}$$

By plugging Eq. (A:b1) into the A:ak th equation enable us to determine the electric current flowing into a k th branch of the integrator as follows:

$$I_{A_k} = \frac{1}{R_{A_k}^{ei}} \left[V_{A_k} - V_0 - \frac{\sum_{k=1}^{M} \frac{R_T^{ei}}{R_{A_k}^{ei}} V_{A_k} - V_0 \sum_{k=1}^{M} \frac{R_T^{ei}}{R_{A_k}^{ei}}}{1 + \sum_{k=1}^{M} \frac{R_T^{ei}}{R_{A_k}^{ei}}} - \left(1 - \frac{\sum_{k=1}^{M} \frac{R_T^{ei}}{R_{A_k}^{ei}}}{1 + \sum_{k=1}^{M} \frac{R_T^{ei}}{R_{A_k}^{ei}}} \right) R_T^{e} I_T^{inje} + \frac{\sum_{k=1}^{M} \frac{R_T^{ei}}{R_{A_k}^{ei}} R_{A_k}^{e} I_{A_k}^{inje}}{1 + \sum_{k=1}^{M} \frac{R_T^{ei}}{R_{A_k}^{ei}}} - R_{A_k}^{e} I_{A_k}^{inje} \right] \qquad \text{(A:b2)}$$

Hence, coupling Eq. (A:b2) with the ones below:

$$V_{A_k} = E_{A_k}^{*} - R_{A_k}^{*} I_{A_k} \qquad \text{(A:b3)}$$

$$E_{A_k}^{*} = R_{A_k} I_{A_k}^{I}, \qquad \text{(A:b4)}$$

enable us to obtain an equation to describe the change in the membrane potential in each of the branches of the integrator:

$$\frac{dV_{A_k}}{dt}=\frac{1}{\tau_m}\left[R_{A_k}{I_{A_k}}^{I}-\left(1+\frac{R_{A_k}}{{R_{A_k}}^{ei}}\right)V_{A_k}+\left(\frac{\sum_{l=1}^{M}\frac{{R_T}^{ei}}{{R_{A_l}}^{ei}}V_{A_l}}{1+\sum_{l=1}^{M}\frac{{R_T}^{ei}}{{R_{A_l}}^{ei}}}\right)\frac{R_{A_k}}{{R_{A_k}}^{ei}}+\left(\frac{1}{1+\sum_{l=1}^{M}\frac{{R_T}^{ei}}{{R_{A_l}}^{ei}}}\right)\frac{R_{A_k}}{{R_{A_k}}^{ei}}V_0+V_{EXTRA}\right] \quad \text{(A:b5)}$$

$$V_{EXTRA}=\frac{R_{A_k}}{{R_{A_k}}^{ei}}\left[\left(1-\frac{\sum_{l=1}^{M}\frac{{R_T}^{ei}}{{R_{A_l}}^{ei}}}{1+\sum_{l=1}^{M}\frac{{R_T}^{ei}}{{R_{A_l}}^{ei}}}\right){R_T}^{e}I_T^{inje}+\left({R_{A_k}}^{e}I_{A_k}^{inje}-\frac{\sum_{l=1}^{M}\frac{{R_T}^{ei}}{{R_{A_l}}^{ei}}{R_{A_l}}^{e}I_{A_l}^{inje}}{1+\sum_{l=1}^{M}\frac{{R_T}^{ei}}{{R_{A_l}}^{ei}}}\right)\right] \quad \text{(A:b6)}$$

From Eqs. (A:aM+2) and (A:aM+4), the following expressions of the electric currents are obtained:

$$I_1^{O}=\frac{V_0-E_T^{*}}{R_T^{*}} \quad \text{(A:b7)}$$

$$I_1^{e}=I_1^{i}=\frac{V_0-V_1}{{R_T}^{ei}} \quad \text{(A:b8)}$$

The equation describing the dynamics of the membrane potential in the last compartment of the integrator is obtained by inserting Eqs. (A:b7) and (A:b8) into Eq. (A:aM+3). Thus, we have:

$$\frac{dV_0}{dt}=\frac{1}{\tau_m}\left[R_T{I_0}^{I}+\frac{R_T\sum_{l=1}^{M}\frac{V_{A_l}}{{R_{A_l}}^{ei}}}{1+\sum_{l=1}^{M}\frac{{R_T}^{ei}}{{R_{A_l}}^{ei}}}-\left(1+\frac{R_T}{{R_T}^{ei}}+\frac{R_T\sum_{l=1}^{M}\frac{1}{{R_{A_l}}^{ei}}}{1+\sum_{l=1}^{M}\frac{{R_T}^{ei}}{{R_{A_l}}^{ei}}}\right)V_0+\frac{R_T}{{R_T}^{ei}}V_1+V_{EXTRA}\right] \quad \text{(A:b9)}$$

$$V_{EXTRA}=-\left(\frac{\sum_{l=1}^{M}\frac{R_T}{{R_{A_l}}^{ei}}}{1+\sum_{l=1}^{M}\frac{{R_T}^{ei}}{{R_{A_l}}^{ei}}}\right){R_T}^{e}I_T^{inje}-\frac{\sum_{l=1}^{M}\frac{R_T}{{R_{A_l}}^{ei}}{R_{A_l}}^{e}I_{A_l}^{inje}}{1+\sum_{l=1}^{M}\frac{{R_T}^{ei}}{{R_{A_l}}^{ei}}}+\frac{R_T}{{R_T}^{ei}}{R_T}^{e}I_T^{inje} \quad \text{(A:b10)}$$

B: Model of the propagator

The propagator (Figure 1-A2) refers to an electrotonic device along which an AP can propagate. Since the morphometry happens to be non-uniform within a compartment of the propagator, we assume that all compartments can be divided into two sub-compartments (upper and lower parts). Thus, by applying the Kirchhoff's voltage law for all meshes of the propagator's equivalent electrical

circuit (Figure 2-B), the following equations are obtained:

$$-V_0 + V_{T_1} + R_{T_1}{}^{Ue} I_{T_1}{}^{Ue} + R_{T_1}{}^{Ue} I_{T_1}{}^{inje} + R_{T_1}{}^{Ui} I_{T_1}{}^{Ui} = 0 \quad \text{(B:a1)}$$

$$-V_{T_1} + V_{T_2} + R_{T_1}{}^{Le} I_{T_1}{}^{Le} + R_{T_1}{}^{Li} I_{T_1}{}^{Li} + R_{T_2}{}^{Ue} I_{T_2}{}^{Ue} + R_{T_2}{}^{Ue} I_{T_2}{}^{inje} + R_{T_2}{}^{Ui} I_{T_2}{}^{Ui} = 0 \quad \text{(B:a2)}$$

$$-V_{T_2} + V_{T_3} + R_{T_2}{}^{Le} I_{T_2}{}^{Le} + R_{T_2}{}^{Li} I_{T_2}{}^{Li} + R_{T_3}{}^{Ue} I_{T_3}{}^{Ue} + R_{T_3}{}^{Ue} I_{T_3}{}^{inje} + R_{T_3}{}^{Ui} I_{T_3}{}^{Ui} = 0 \quad \text{(B:a3)}$$

. . . .
. . . .
. . . .

$$-V_{T_{k-1}} + V_{T_k} + R_{T_{k-1}}{}^{Le} I_{T_{k-1}}{}^{Le} + R_{T_{k-1}}{}^{Li} I_{T_{k-1}}{}^{Li} + R_{T_k}{}^{Ue} I_{T_k}{}^{Ue} + R_{T_k}{}^{Ue} I_{T_k}{}^{inje} + R_{T_k}{}^{Ui} I_{T_k}{}^{Ui} = 0 \quad \text{(B:ak)}$$

. . . .
. . . .
. . . .

$$-V_{T_{N-1}} + V_{T_N} + R_{T_{N-1}}{}^{Le} I_{T_{N-1}}{}^{Le} + R_{T_{N-1}}{}^{Li} I_{T_{N-1}}{}^{Li} + R_{T_N}{}^{Ue} I_{T_N}{}^{Ue} + R_{T_N}{}^{Ue} I_{T_N}{}^{inje} + R_{T_N}{}^{Ui} I_{T_N}{}^{Ui} = 0 \quad \text{(B:aN-1)}$$

$$-V_{T_N} + V_{T_{N+1}} + R_{T_N}{}^{Le} I_{T_N}{}^{Le} + R_{T_N}{}^{Le} I_{T_N}{}^{inje} + R_{T_N}{}^{Li} I_{T_N}{}^{Li} = 0 \quad \text{(B:aN)}$$

By applying Kirchhoff's current law, the following node equations [Eqs. (B:a1) – (B:aN)]:

$$I_{T_k}{}^{Li} = I_{T_{k+1}}{}^{Ui} \quad \text{(B:aN+1)}$$

$$I_{T_k}{}^{Le} = I_{T_{k+1}}{}^{Ue} \quad \text{(B:aN+2)}$$

$$I_{T_1}{}^{Ue} = I_{T_1}{}^{Ui} \quad \text{(B:aN+3)}$$

$$I_{T_2}{}^{Ue} = I_{T_2}{}^{Ui} \quad \text{(B:aN+4)}$$

$$I_{T_2}{}^{Ui} = I_{T_2}{}^{Ue} = I_{T_1}{}^{Ui} - I_{T_1} \quad \text{(B:aN+5)}$$

$$I_{T_3}{}^{Ui} = I_{T_3}{}^{Ue} = I_{T_1}{}^{Ui} - (I_{T_1} + I_{T_2}) \quad \text{(B:aN+6)}$$

$$I_{T_4}{}^{Ui} = I_{T_4}{}^{Ue} = I_{T_1}{}^{Ui} - (I_{T_1} + I_{T_2} + I_{T_3}) \quad \text{(B:aN+7)}$$

. . . . .

. . . . .

. . . . .

$$I_{T_k}{}^{Ue} = I_{T_k}{}^{Ui} = I_{T_1}{}^{Ui} - \sum_{p=1}^{N-1} I_{T_p} \qquad \text{(B:aN+8)}$$

$$I_{T_{N+1}}{}^{Ue} = I_{T_{N+1}}{}^{Ui} = I_{T_1} - \sum_{p=1}^{N-1} I_{T_p} - I_{T_N} \,, \qquad \text{(B:aN+9)}$$

can be rewritten as follows:

$$-(V_0 - V_{T_1}) + R_{T_1}{}^{Uei} I_{T_1}{}^{Ui} + R_{T_1}{}^{Ue} I_{T_1}{}^{inje} = 0 \qquad \text{(B:b1)}$$

$$-(V_{T_{k-1}} - V_{T_k}) + (R_{T_{k-1}} + R_{T_k}{}^{Uei}) I_{T_k}{}^{Ui} + R_{T_k}{}^{Ue} I_{T_k}{}^{inje} = 0 \qquad \text{(B:b2)}$$

$$-(V_{T_N} - V_{T_{N+1}}) + R_{T_N} I_{T_N}{}^{Ui} - R_{T_N}{}^{Lei} I_{T_N} + R_{T_N}{}^{Le} I_{T_N}{}^{inje} = 0 \qquad \text{(B:b3)}$$

Where $R_{T_k}{}^{Xei} = R_{T_k}{}^{Xe} + R_{T_k}{}^{Xi}$, $X = \{L, U\}$.

The supra indexes "*e*" and "*i*" hold for the extracellular and intracellular spaces. The supra indexes "*U*" and "*L*" hold for the upper part and lower part of every compartment of the propagator. $I_{T_k}{}^{inje}$ stands for an extracellular injection current at the extracellular resistance of the Tth compartment of the propagator. From the above equations, expressions of the currents flowing into particular resistances of the propagator are given as follows:

$$I_{T_1}{}^{Ui} = \frac{V_0 - V_{T_1}}{R_{T_1}{}^{Uei}} - \frac{R_{T_1}{}^{Ue}}{R_{T_1}{}^{Uei}} I_{T_1}{}^{inje} \qquad \text{(B:b4)}$$

$$I_{T_1} = \frac{V_0 - V_{T_1}}{R_{T_1}{}^{Uei}} + \frac{V_{T_2} - V_{T_1}}{R_{T_1}{}^{Lei} + R_{T_2}{}^{Uei}} + \frac{R_{T_2}{}^{Ue}}{R_{T_1}{}^{Lei} + R_{T_2}{}^{Uei}} I_{T_2}{}^{inje} - \frac{R_{T_1}{}^{Ue}}{R_{T_1}{}^{Uei}} I_{T_1}{}^{inje} \qquad \text{(B:b5)}$$

$$I_{T_k} = \frac{V_{T_{k-1}} - V_{T_k}}{R_{T_{k-1}}{}^{Lei} + R_{T_k}{}^{Uei}} + \frac{V_{T_{k+1}} - V_{T_k}}{R_{T_k}{}^{Lei} + R_{T_{k+1}}{}^{Uei}} + \frac{R_{T_{k+1}}{}^{Ue}}{R_{T_k}{}^{Lei} + R_{T_{k+1}}{}^{Uei}} I_{T_{k+1}}{}^{inje} - \frac{R_{T_k}{}^{Ue}}{R_{T_{k-1}}{}^{Lei} + R_{T_k}{}^{Uei}} I_{T_k}{}^{inje} \qquad \text{(B:b6)}$$

$$2 \le k \le N-1$$

$$I_{T_N} = \frac{V_{T_{N-1}} - V_{T_N}}{R_{T_{N-1}}^{Lei} + R_{T_N}^{Uei}} + \frac{V_{T_{N+1}} - V_{T_N}}{R_{T_N}^{Lei}} + \frac{R_{T_N}^{Le}}{R_{T_N}^{Lei}} I_{T_{N+1}}^{inje} - \frac{R_{T_N}^{Ue}}{R_{T_{N-1}}^{Lei} + R_{T_N}^{Uei}} I_{T_N}^{inje} \qquad \text{(B:b7)}$$

$$I_{T_N}^{Li} = \frac{V_{T_N} - V_{T_{N+1}}}{R_{T_N}^{Lei}} - \frac{R_{T_N}^{Le}}{R_{T_N}^{Lei}} I_{T_{N+1}}^{inje} \qquad \text{(B:b8)}$$

The expression of electric voltage through the membrane in the k th compartment is defined as follows:

$$V_{T_k} = E_{T_k}^{*} + R_{T_k}^{*} I_{T_k} \qquad \text{(B:b9)}$$

After some algebraic manipulations, Eqs. (B:b4) – (B:b9) enable us to find the final expressions for the membrane potentials at all compartments of the propagator:

$$\frac{dV_{T_1}}{dt} = \frac{1}{\tau_m}\left[R_{T_1} I_{T_1}^{I} + \frac{R_{T_1}}{R_{T_1}^{Uei}} V_0 - \left(1 + \frac{R_{T_1}}{R_{T_1}^{Uei}} + \frac{R_{T_1}}{R_{T_1}^{Lei} + R_{T_2}^{Uei}}\right) V_{T_1} + \frac{R_{T_1}}{R_{T_1}^{Lei} + R_{T_2}^{Uei}} V_{T_2} + V_{EXTRA_1} \right] \qquad \text{(B:b10)}$$

$$V_{EXTRA_1} = R_{T_1}\left(\frac{R_{T_2}^{Ue}}{R_{T_1}^{Lei} + R_{T_2}^{Uei}} I_{T_2}^{inje} - \frac{R_{T_1}^{Ue}}{R_{T_1}^{Uei}} I_{T_1}^{inje} \right) \qquad \text{(B:b11)}$$

$$\frac{dV_{T_k}}{dt} = \frac{1}{\tau_m}\left[R_{T_k} I_{T_k}^{I} + \frac{R_{T_k}}{R_{T_{k-1}}^{Lei} + R_{T_k}^{Uei}} V_{T_{k-1}} - \left(1 + \frac{R_{T_k}}{R_{T_{k-1}}^{Lei} + R_{T_k}^{Uei}} + \frac{R_{T_k}}{R_{T_k}^{Lei} + R_{T_{k+1}}^{Uei}}\right) V_{T_k} + \frac{R_{T_k}}{R_{T_k}^{Lei} + R_{T_{k+1}}^{Uei}} V_{T_{k+1}} + V_{EXTRA_k} \right] \qquad \text{(B:b12)}$$

$$V_{EXTRA_k} = R_{T_k}\left(\frac{R_{T_{k+1}}^{Ue}}{R_{T_k}^{Lei} + R_{T_{k+1}}^{Uei}} I_{T_{k+1}}^{inje} - \frac{R_{T_k}^{Ue}}{R_{T_{k-1}}^{Lei} + R_{T_k}^{Uei}} I_{T_k}^{inje} \right) \qquad \text{(B:b13)}$$

$$2 \le k \le N-1$$

$$\frac{dV_{T_N}}{dt} = \frac{1}{\tau_m}\left[R_{T_N} I_{T_N}^{I} + \frac{R_{T_N}}{R_{T_{N-1}}^{Lei} + R_{T_N}^{Uei}} V_{T_{N-1}} - \left(1 + \frac{R_{T_N}}{R_{T_{N-1}}^{Lei} + R_{T_N}^{Uei}} + \frac{R_{T_N}}{R_{T_N}^{Lei}}\right) V_{T_N} + \frac{R_{T_N}}{R_{T_N}^{Lei}} V_{T_{N+1}} + V_{EXTRA_N} \right] \qquad \text{(B:b14)}$$

$$V_{EXTRA_N} = R_{T_N}\left(\frac{R_{T_N}^{Le}}{R_{T_N}^{Lei}} I_{T_{N+1}}^{inje} - \frac{R_{T_N}^{Ue}}{R_{T_{N-1}}^{Lei} + R_{T_N}^{Uei}} I_{T_N}^{inje} \right) \qquad \text{(B:b15)}$$

C: Model of the 3D-connector

The 3D-connector (Figure 1-A1) refers to an electrotonic device that links three particular building blocks to simulate a point of branch bifurcations. Every branch of the 3D-connector receives and generates both input and output electric potentials. Without losing generality, we will assume that the 3D-connector contains two inputs and one single output. By applying the Kirchhoff's laws within all meshes of the 3D-connector's equivalent electrical circuit (Figure 2-C), the following equations are obtained:

$$-V_1^I + R_1^{ei} I_1^I + R_1^e I_1^{inje} + V_M = 0 \qquad \text{(C:a1)}$$

$$-V_2^I + R_2^{ei} I_2^I + R_2^e I_2^{inje} + V_M = 0 \qquad \text{(C:a2)}$$

$$-V^O + R_O^{ei} I_O^I + R_O^e I_O^{inje} + V_M = 0 \qquad \text{(C:a3)}$$

$$I_M = I_1^I + I_2^I + I_O^I \qquad \text{(C:a4)}$$

$$-V_M + R_M^* I_M + E_M^* = 0 \qquad \text{(C:a5)}$$

$$E_M^* = R_M^* I_M^I \qquad \text{(C:a6)}$$

Where $R_\chi^{ei} = R_\chi^e + R_\chi^i$, $\chi = \{0,1,2\}$.

The supra indexes "*e*" and "*i*" hold for the extracellular and intracellular spaces. I_χ^I stands for a current entering the three branches of the integrator. I_χ^{inje} stands for an extracellular injection current at the extracellular resistance of the three branches of the 3D-connector. From the above equations, expressions of currents flowing into the extra/intra cellular resistances of the 3D connector are given as follows:

$$I_1^I = \frac{V_1^I - V_M - R_1^e I_1^{inje}}{R_1^{ei}} \qquad \text{(C:a7)}$$

$$I_2^I = \frac{V_2^I - V_M - R_2^e I_2^{inje}}{R_2^{ei}} \qquad \text{(C:a8)}$$

$$I_O^I = \frac{V^O - V_M - R_O^e I_O^{inje}}{R_O^{ei}} \qquad \text{(C:a9)}$$

From the above equations, we obtained an equation which describes the changes in the membrane potential in the 3D-connector:

$$\frac{dV_M}{dt} = \frac{1}{\tau_m}\left[R_M I_M^I + \frac{R_M}{R_1^{ei}} V_1^I + \frac{R_M}{R_2^{ei}} V_2^I + \frac{R_M}{R_O^{ei}} V^O - (1 + \frac{R_M}{R_1^{ei}} + \frac{R_M}{R_2^{ei}} + \frac{R_M}{R_O^{ei}}) V_M + V_{EXTRA} \right] \qquad \text{(C:b1)}$$

$$V_{EXTRA} = -\frac{R_M}{R_1^{ei}} R_1^e I_1^{inje} - \frac{R_M}{R_2^{ei}} R_2^e I_2^{inje} - \frac{R_M}{R_O^{ei}} R_O^e I_O^{inje} \qquad \text{(C:b2)}$$

D: Model of the collector

The collector (Figure 1-A2 and B2) represents an electrotonic device that collects many inputs coming from other devices. Based on its equivalent electrical circuit, represented in the Figure 2-D, we were able to obtain the following equations:

$$V_S - R_S{}^{ei} I - R_S{}^e I_S^{inje} - R_{S_1}{}^{ei} I_{S_1} - R_{S_1}{}^e I_{S_1}^{inje} + V_{S_1} = 0 \qquad \text{(D:a1)}$$

$$V_S - R_S{}^{ei} I - R_S{}^e I_S^{inje} - R_{S_2}{}^{ei} I_{S_2} - R_{S_2}{}^e I_{S_2}^{inje} + V_{S_2} = 0 \qquad \text{(D:a2)}$$

. . . . .
. . . . .
. . . . .

$$V_S - R_S{}^{ei} I - R_S{}^e I_S^{inje} - R_{S_k}{}^{ei} I_{S_k} - R_{S_k}{}^e I_{S_k}^{inje} + V_{S_k} = 0 \qquad \text{(D:ak)}$$

. . . . .
. . . . .
. . . . .

$$V_S - R_S{}^{ei} I - R_S{}^e I_S^{inje} - R_{S_M}{}^{ei} I_{S_M} - R_{S_M}{}^e I_{S_M}^{inje} + V_{S_M} = 0 \qquad \text{(D:aM)}$$

$$I = \sum_{k=1}^{M} I_{S_k} \qquad \text{(D:aM+1)}$$

$$V_S - E_S{}^* - R_S{}^* I = 0 \qquad \text{(D:aM+2)}$$

$$V_{S_k} + R_{S_k}{}^{*} I_k - E_{S_k}{}^{*} = 0 \tag{D:aM+3}$$

$$V_{S_k} + R_{T_k}{}^{e} I_k{}^{e} + R_{T_k}{}^{e} I_k{}^{inje} + R_{T_k}{}^{i} I_k{}^{i} - V_{T_k} = 0 \tag{D:aM+4}$$

$$I_{S_k} = I_k + I_k{}^{e} = I_k + I_k{}^{i} \tag{D:aM+5}$$

Where $R_S{}^{ei} = R_S{}^{e} + R_S{}^{i}$.

I_{S_k} represents currents that flow into a branch of the collector. The supra indexes "*e*" and "*i*" hold for the extracellular and intracellular spaces. $I_{S_k}^{inje}$ stands for an extracellular injection current at the extracellular resistance of the k th branch of the collector. I_S^{inje} stands for an extracellular injection current at the extracellular resistance of the soma compartment of the collector. After dividing each k th equation by $R_{S_k}{}^{ei}$ and summing up all equations, the following expression of the electric current could be obtained:

$$I = \frac{\sum_{k=1}^{M} \frac{V_{S_k}}{R_{S_k}{}^{ei}} - V_S \sum_{k=1}^{M} \frac{1}{R_{S_k}{}^{ei}} - I_S^{inje} R_S{}^{e} \sum_{k=1}^{M} \frac{1}{R_{S_k}{}^{ei}} - \sum_{k=1}^{M} \frac{I_{S_k}^{inje} R_{S_k}{}^{e}}{R_{S_k}{}^{ei}}}{1 + R_S{}^{ei} \sum_{k=1}^{M} \frac{1}{R_{S_k}{}^{ei}}} \tag{D:b1}$$

From Eqs. (D:aM+2) and (D:b1), the dynamics of the membrane potential in the collector are governed by the equation below:

$$\frac{dV_S}{dt} = \frac{1}{\tau_m} \left[R_S I_S{}^{I} + \frac{R_S \sum_{l=1}^{M} \frac{V_{S_l}}{R_{S_l}{}^{ei}}}{1 + \sum_{l=1}^{M} \frac{R_S{}^{ei}}{R_{S_l}{}^{ei}}} - \left(1 + \frac{R_S \sum_{l=1}^{M} \frac{1}{R_{S_l}{}^{ei}}}{1 + \sum_{l=1}^{M} \frac{R_S{}^{ei}}{R_{S_l}{}^{ei}}} \right) V_S + V_{EXTRA} \right] \tag{D:b2}$$

$$V_{EXTRA} = -\frac{R_S}{R_S{}^{ei}} \frac{I_S^{inje} R_S{}^{e} \sum_{l=1}^{M} \frac{1}{R_{S_l}{}^{ei}}}{\frac{1}{R_S{}^{ei}} + \sum_{l=1}^{M} \frac{1}{R_{S_l}{}^{ei}}} - \frac{R_S}{R_S{}^{ei}} \frac{\sum_{l=1}^{M} \frac{I_{S_k}^{inje} R_{S_l}{}^{e}}{R_{S_l}{}^{ei}}}{\frac{1}{R_S{}^{ei}} + \sum_{l=1}^{M} \frac{1}{R_{S_l}{}^{ei}}} \tag{D:b3}$$

The following expressions of currents are obtained from Eqs. (D:aM+2), (D:aM+3), (D:aM+4), (D:aM+5) and (D:ak):

$$I_{S_k} = \frac{E_S^{\,*} - V_{S_k}}{R_S^{\,*}} + \frac{V_{T_k} - V_{S_k} - R_{T_k}^{\,e} I_k^{\,inje}}{R_{T_k}^{\,ei}} \tag{D:b4}$$

After inserting Eq. (D:b4) into the D:bk th equation and some algebraic calculations, the dynamics of membrane potential at the k th entrance of the collector is governed by the following equation:

$$\frac{dV_{S_k}}{dt} = \frac{1}{\tau_m}\left[R_{S_k} I_{S_k}^{\,I} + \frac{R_{S_k}}{R_{T_k}^{\,ei}} V_{T_k} - \left(1 + \frac{R_{S_k}}{R_{T_k}^{\,ei}} + \frac{R_{S_k}}{R_{S_k}^{\,ei}}\right) V_{S_k} + \left(\frac{\sum_{l=1}^{M} \frac{R_S^{\,ei}}{R_{S_l}^{\,ei}} V_{S_l}}{1 + \sum_{l=1}^{M} \frac{R_S^{\,ei}}{R_{S_l}^{\,ei}}} \right) \frac{R_{S_k}}{R_{S_k}^{\,ei}} + \left(\frac{R_{S_k}}{1 + \sum_{l=1}^{M} \frac{R_S^{\,ei}}{R_{S_l}^{\,ei}}} \right) \frac{V_S}{R_{S_k}^{\,ei}} + V_{EXTRA} \right] \tag{D:b5}$$

$$V_{EXTRA} = -R_{S_k} \frac{R_{T_k}^{\,e}}{R_{T_k}^{\,ei}} I_k^{\,inje} - \frac{R_{S_k}}{R_{S_k}^{\,ei}} \frac{I_S^{inje} R_S^{\,e} \sum_{l=1}^{M} \frac{1}{R_{S_l}^{\,ei}}}{\frac{1}{R_S^{\,ei}} + \sum_{l=1}^{M} \frac{1}{R_{S_l}^{\,ei}}} - \frac{R_{S_k}}{R_{S_k}^{\,ei}} \frac{\sum_{l=1}^{M} \frac{I_{S_k}^{inje} R_{S_l}^{\,e}}{R_{S_l}^{\,ei}}}{\frac{1}{R_S^{\,ei}} + \sum_{l=1}^{M} \frac{1}{R_{S_l}^{\,ei}}} \tag{D:b6}$$

Here, $I_{S_k}^{\,I} = I_{S_k}^{\,S} + I_{S_k}^{\,i}$ represents the sum of the synaptic and ionic currents.

3. Model of the LFP

The equivalent equations for every electrotonic device have already been obtained in the "Model of building blocks" part (appendix 2); therefore, we only used henceforth the "B: Model of the propagator" to exemplify how to create a model of LFP. A similar analysis can be applied to obtain the LFP generated by other types of electrotonic devices. The LFP are defined for the situation of a zero extracellular stimulation; hence, the injection current at the ECS in the equations of propagator were ignored.

In the Figure 4, R_i^e shows the i th resistance of the ECS which is in between the i th and $i+1$ th compartment, U_i shows the voltage difference at the resistance R_i^e. The LFP is calculated by the equation $U_i = R_i^e I_i$. Therefore, we just need to deduct the equations of extracellular currents I_i. In the case of the propagator, the extracellular currents I_i along the compartment are defined by the Eqs. (B:aN+1) – (B:aN+9). Eqs. (B:b4) – (B:b8) defined the membrane currents in the compartments, so we can get the extracellular currents I_i at the compartment by the following equations:

$$I_{T_2}^{Ui} = I_{T_2}^{Ue} = I_{T_1}^{Ui} - I_{T_1} = -\frac{V_{T_2} - V_{T_1}}{R_{T_1}^{Lei} + R_{T_2}^{Uei}} \quad \text{(E:b1)}$$

. . . . .

$$I_{T_k}^{Ue} = I_{T_k}^{Ui} = I_{T_1}^{Ui} - \sum_{p=1}^{N-1} I_{T_p} = -\frac{V_{T_{k+1}} - V_{T_k}}{R_{T_k}^{Lei} + R_{T_{k+1}}^{Uei}} \quad \text{(E:b2)}$$

Therefore, the LFP can be defined from the extracellular potentials: $U_{T_k}^{Ue} = I_{T_k}^{Ue}\left(R_{T_k}^{Le} + R_{T_{k+1}}^{Ue}\right)$.

Figure and table legends

Figure 1. The general multi-compartmental model for neurons

A1 – The morphometry of a PCL5 neuron. **A2** – The devices of the model of PCL5 neurons. **B1** – The morphometry of a spiny stellate neuron. **B2** – The devices of the model of spiny stellate neurons. In **A2** and **B2**, the letters **I**, **P**, **3D** and **C** denote integrator, propagator, 3D-connector, and collector, respectively. The integrator is defined as a device that possesses many tuft branches with heterogeneous impedances, receives a huge amount of input voltages, and produces a single output voltage in the last compartment of the integrator which is used as the input into another building block. The propagator refers to a device which propagates APs. The propagator is composed of several compartments which are, in principle, non-uniform. 3D-connector is useful to connect three other different electrotonic devices. The collector represents the device that collects different inputs. Figure 1-B1 has been modified from da Costa & Martin (2011).

Figure 2. The equivalent electrical circuits of the general multi-compartmental model

The equivalent electrical circuits for **A**: the integrator, **B**: the propagator, **C**: the 3D-connector, and **D**: the collector. The French grey rectangle shows the resistance of the ICS, the Oxford grey rectangle shows the resistance of the ECS and the dark black rectangle shows the membrane resistance. The electromotive forces are caused by the ionic currents across the membrane. **A** – The electrical circuit of integrator contains two parts: the first part possesses many tufted branches with heterogeneous impedances and receives a huge amount of inputs, and the second part produces a single output voltage in the last compartment of the integrator to be used as input in another device. **B** – The electrical circuit of the propagator. The two inputs to this device can come from any other electrotonic devices. The electrical circuit of the propagator is composed of several compartments and all compartments have been divided into two parts: the upper part and the lower part. **C** – The electrical circuit of the 3D-connector, a device that serve to connect three other electrotonic devices. **D** – The electrical circuit of the collector, a device that collects several inputs which results from the outputs of other electrotonic devices. The mathematics equations that describe the dynamics of electric potentials in these devices are shown in Appendix-2 (integrator – A, propagator –B, 3D-connector – C, and D – collector).

Figure 3. A simple model for AP back-propagation in PCL5

Left: A simple model of PCL5 comprising an integrator with a single branch, a propagator made of ten compartments, and a collector which has a single input from the propagator. Right: **A** – The propagator of the PCL5 neuron has ten regions of interest (ROI), named compartments. **B1** – Every compartment of the propagator was approximated by a slender body with a particular diameter and length. **B2** – The collector was approximated by a sphere with a particular diameter.

Figure 4. The LFP generated by the PCL5

A –The strategy used to simulate the LFP for our PCL5 model. LFP signals were represented as the electric potential differences respect to a common reference electrode near the distal trunk in the ECS. The voltage drops on the ECS resistances were used to represent the LFP at each electrode. R_i^e stands for the i th resistance of the ECS, which is between the i th and $i+1$ th compartment, U_i stands for the voltage across resistance R_i^e. **B** – A detailed diagram of the equivalent electric circuit.

Figure 5. A model for the extracellular current injection

A – The original electric circuit containing the resistances of the ECS. **B** – An extracellular current injection source in parallel with resistance of the ECS. **C** – The equivalent circuit in the frequency domain.

Figure 6. A train of APs from a somatic intracellular stimulation

The propagation of an AP train from the soma to the distal trunk is shown for the cases of zero (top) and nonzero (bottom) ECS resistance. We injected a 200 pA current into the soma from 0 ms to 150 ms. The amplitude of the first AP in both panels was larger than the amplitude of any other subsequent APs. The amplitudes of APs in both cases, i.e. zero and nonzero ECS resistance, are almost the same. The frequency/rate of APs were large in the case of zero ECS resistance.

Figure 7. The effects of the ECS resistance on a back-propagating AP

Two singles APs recorded during the same time window but under different situations (i.e. zero and nonzero ECS resistance) are compared.

Figure 8. The amplitude decay and peak delay curves for back-propagating APs

A – The experimental data of decay and delay curves for PCL5 APs, which were

digitalized from the original figures in three previous studies (Stuart and Sakmann, 1994; Gulledge and Stuart, 2003; Bar-Yehuda et al., 2008). We averaged the data to obtain the most likelihood values for the decay and delays curves (continuous lines). In order to obtain values for distant sites from the soma, we extended that averaged data by a lineal interpolation method (dashed lines). B – A comparison of the decay and delay curves for the two simulated APs with the averaged data.

Figure 9. The LFP and CSD analysis

The back-propagating membrane potentials through all compartment of the propagator of the PCL5 are shown on the top-left panel. The particular injection protocol (square pulse current of 200 pA into the soma for a duration of 5 ms) caused this neuron type to generate a single AP. The LFP generated by such a back-propagating AP (top-right). A color panel with the spatiotemporal CSD pattern (bottom-left), which was calculated from the LFPs using the iCSD method. This pattern was very close to those observed experimentally by Bereshpolova et al. (2007). The time series with the multipolar moments are shown on the bottom-right, i.e. the monopoles, the dipoles and the quadrupoles.

Figure 10. The membrane potentials caused by the current injection in the ECS

Four positions (soma and proximal/middle/distal trunk) were chosen to illustrate the neuronal response to current injection in the ECS. The amplitude of the injected current was adjusted at all four locations to keep a similar firing frequency/rate.

Figure 11. The spatial profile for the current injection

The exponential-like relationship between the required amplitudes for the current injection to produce a same output pattern in this type of neuron along the PCL5 trunk.

Figure 12. The RC circuit

The original electric circuit (left) for the cell's membrane is shown on the left, it is constituted by a RC circuit in parallel with a membrane current source. The symbols R_m and C stand for the membrane resistance and capacitance, respectively. In the frequency domain configuration, an equivalent complex resistance of the circuit is defined as $R_m^* = \frac{R_m}{1 + j\omega\tau}$, where $\tau = R_m C$ represents the membrane time constant. In the frequency domain, such an electric circuit is equivalent to a parallel circuit with a

current source and a complex resistance (middle). By means of the Thevenin equivalent theorem, the parallel circuit with a current source and a resistance can be transformed into a serial circuit with a electromotive force and a resistance (right).

Table 1. The geometrical parameters of the PCL5

The statistics were performed from sixteen PCsL5 with different lengths and diameters. The mean values and standard deviations (SD) of the geometrical parameters for all compartments of the integrator, propagator, and collector are shown.

Figure 1

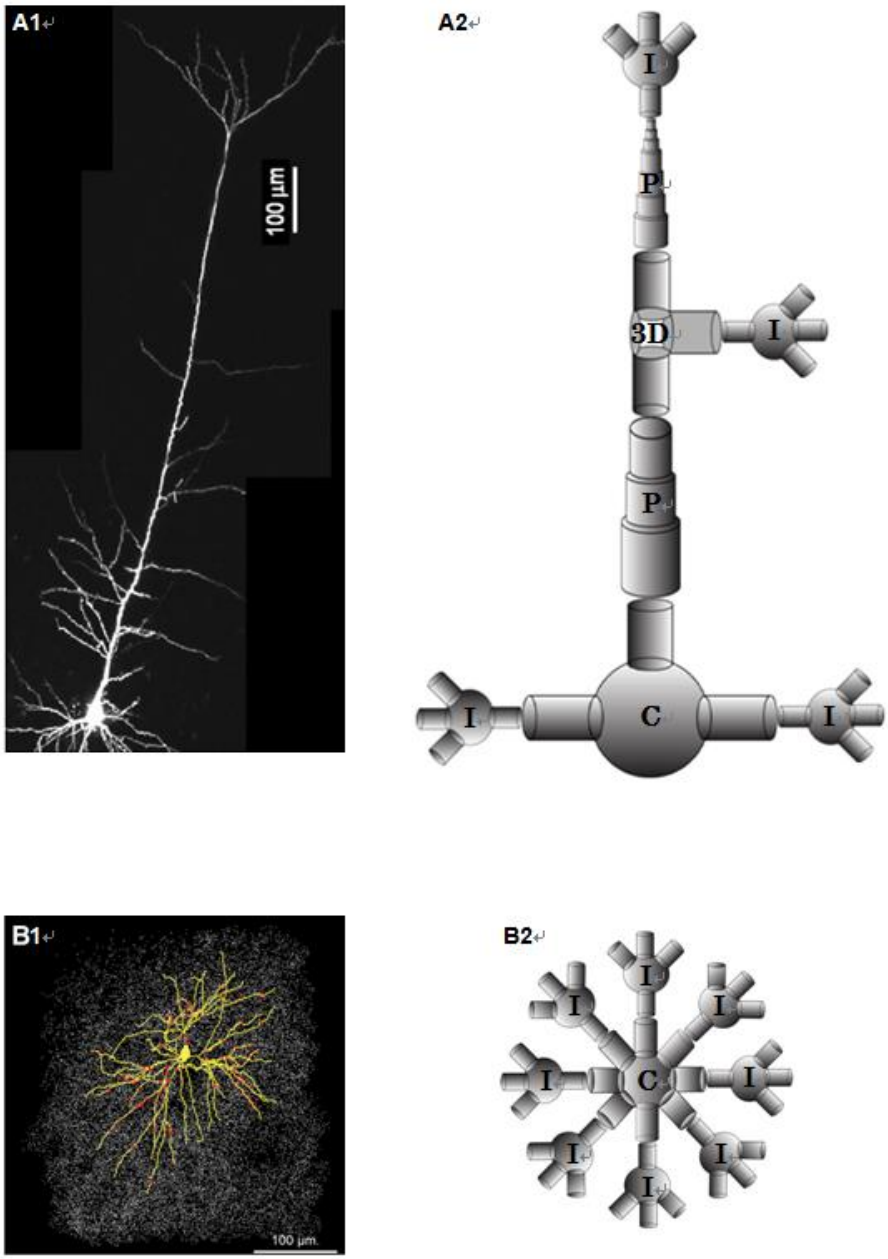

Figure 2-A

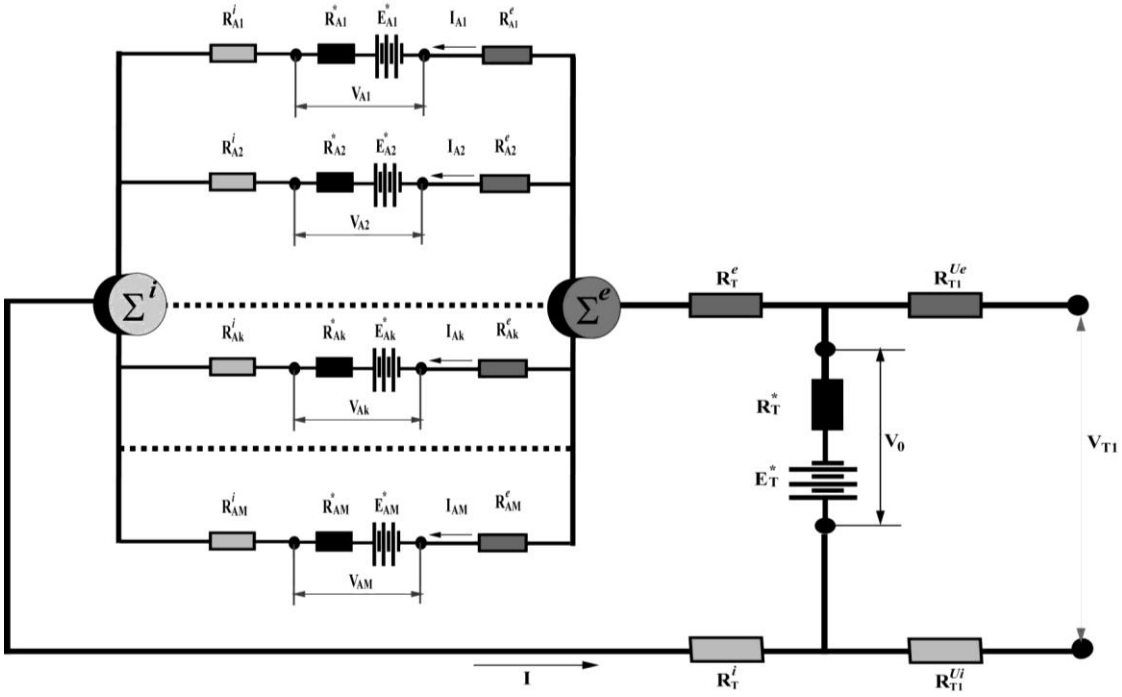
R^{i}_{A1}
R^{*}_{A1}
E^{*}_{A1}
I_{A1}
R^{e}_{A1}
V_{A1}
R^{i}_{A2}
R^{*}_{A2}
E^{*}_{A2}
I_{A2}
R^{e}_{A2}
V_{A2}
Σ^{i}
Σ^{e}
R^{i}_{Ak}
R^{*}_{Ak}
E^{*}_{Ak}
I_{Ak}
R^{e}_{Ak}
V_{Ak}
R^{i}_{AM}
R^{*}_{AM}
E^{*}_{AM}
I_{AM}
R^{e}_{AM}
V_{AM}
R^{e}_{T}
R^{Ue}_{T1}
R^{*}_{T}
V_{0}
V_{T1}
E^{*}_{T}
I
R^{i}_{T}
R^{Ui}_{T1}

Figure 2-B

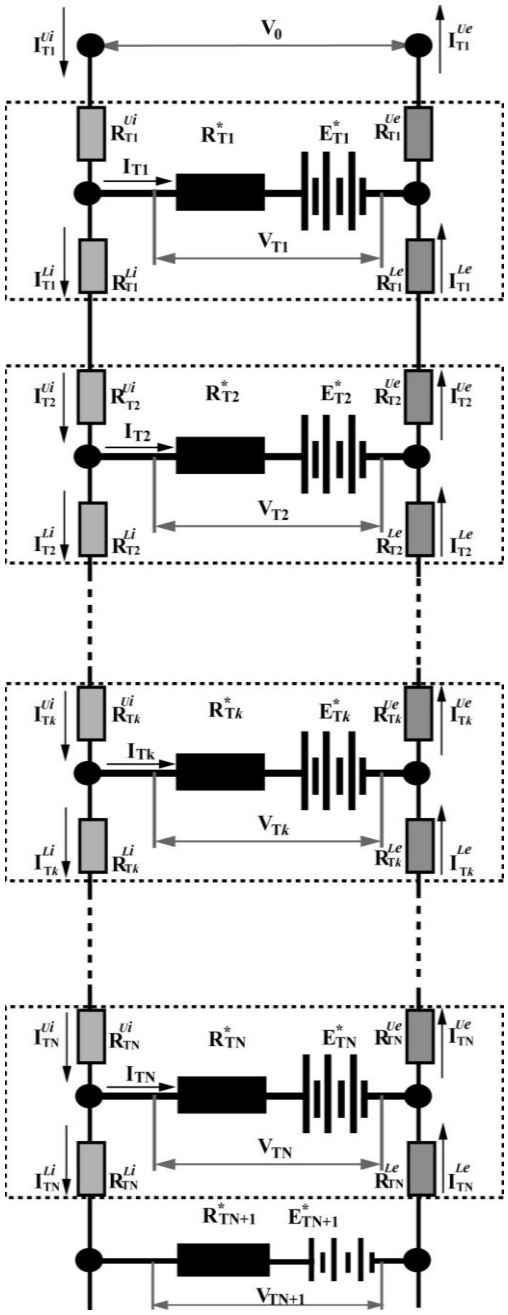
V0
RT1*
ET1*
IT1
VT1
RT2*
ET2*
IT2
VT2
RTk*
ETk*
ITk
VTk
RTN*
ETN*
ITN
VTN
RTN+1*
ETN+1*
VTN+1

Figure 2-C

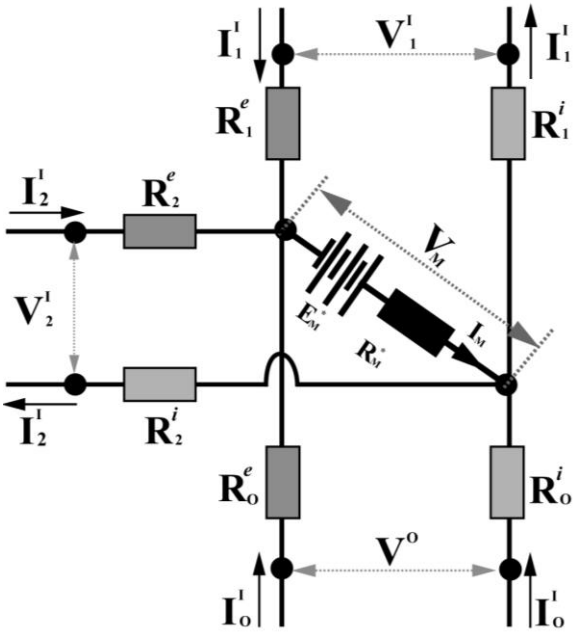
I_1^I
V_1^I
I_1^I
R_1^e
R_1^i
I_2^I
R_2^e
V_M
V_2^I
E_M^*
I_M
R_M^*
I_2^I
R_2^i
R_O^e
R_O^i
V^O
I_O^I
I_O^I

Figure 2-D

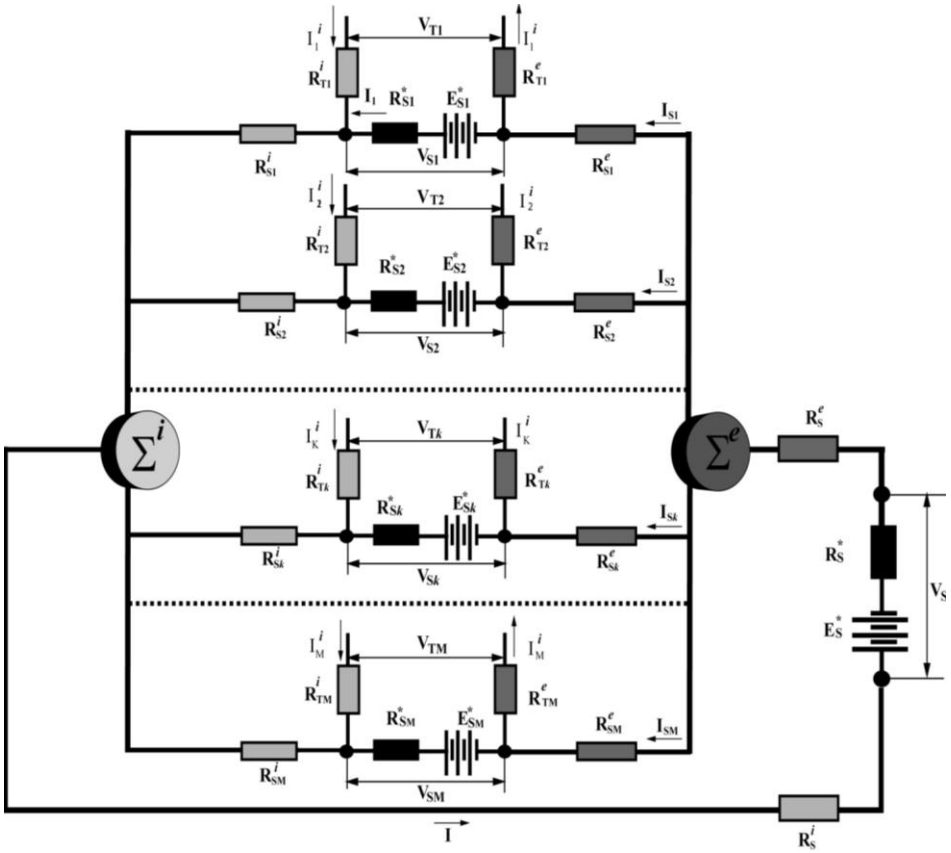
V_{T1}
V_{T2}
V_{Tk}
V_{TM}
V_{S1}
V_{S2}
V_{Sk}
V_{SM}
I_1
I_{S1}
I_{S2}
I_{Sk}
I_{SM}
I
Σ^i
Σ^e
R^*_{S1}
R^*_{S2}
R^*_{Sk}
R^*_{SM}
E^*_{S1}
E^*_{S2}
E^*_{Sk}
E^*_{SM}
R^*_S
E^*_S
V_S
R^e_S
R^i_S

Figure 3

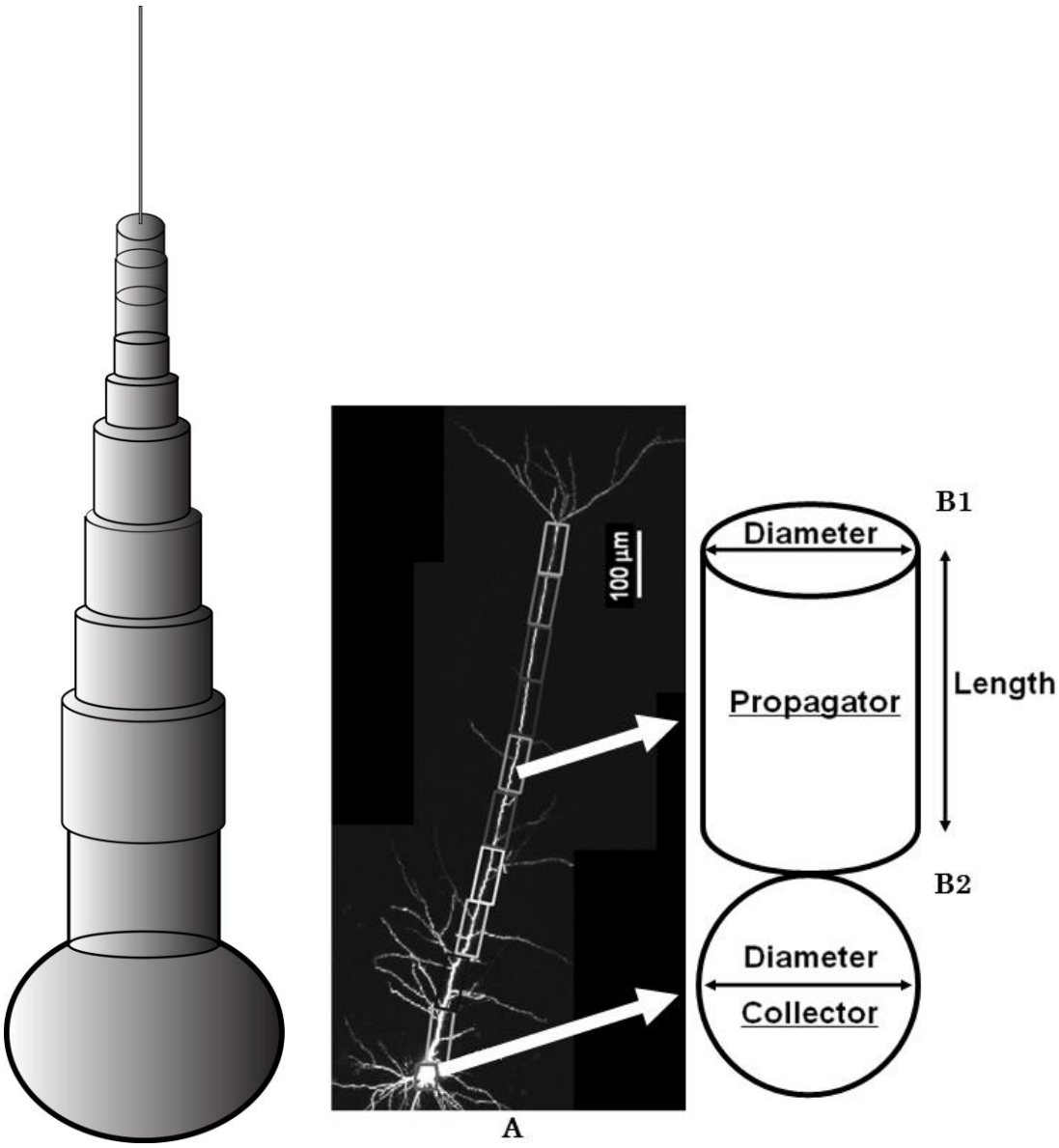
100 µm
Diameter
Propagator
Length
Diameter
Collector
B1
B2
A

Figure 4

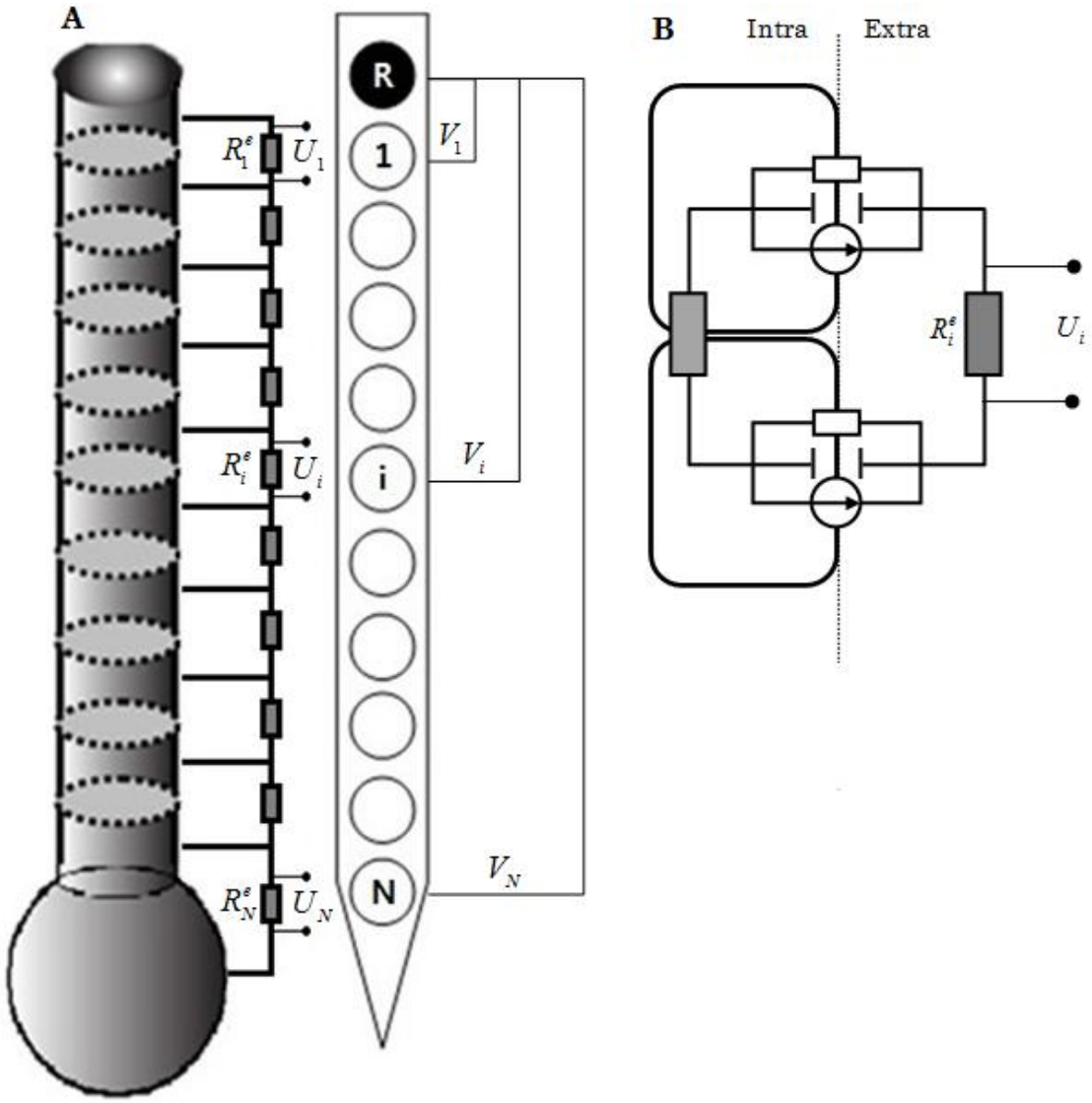

Figure 5

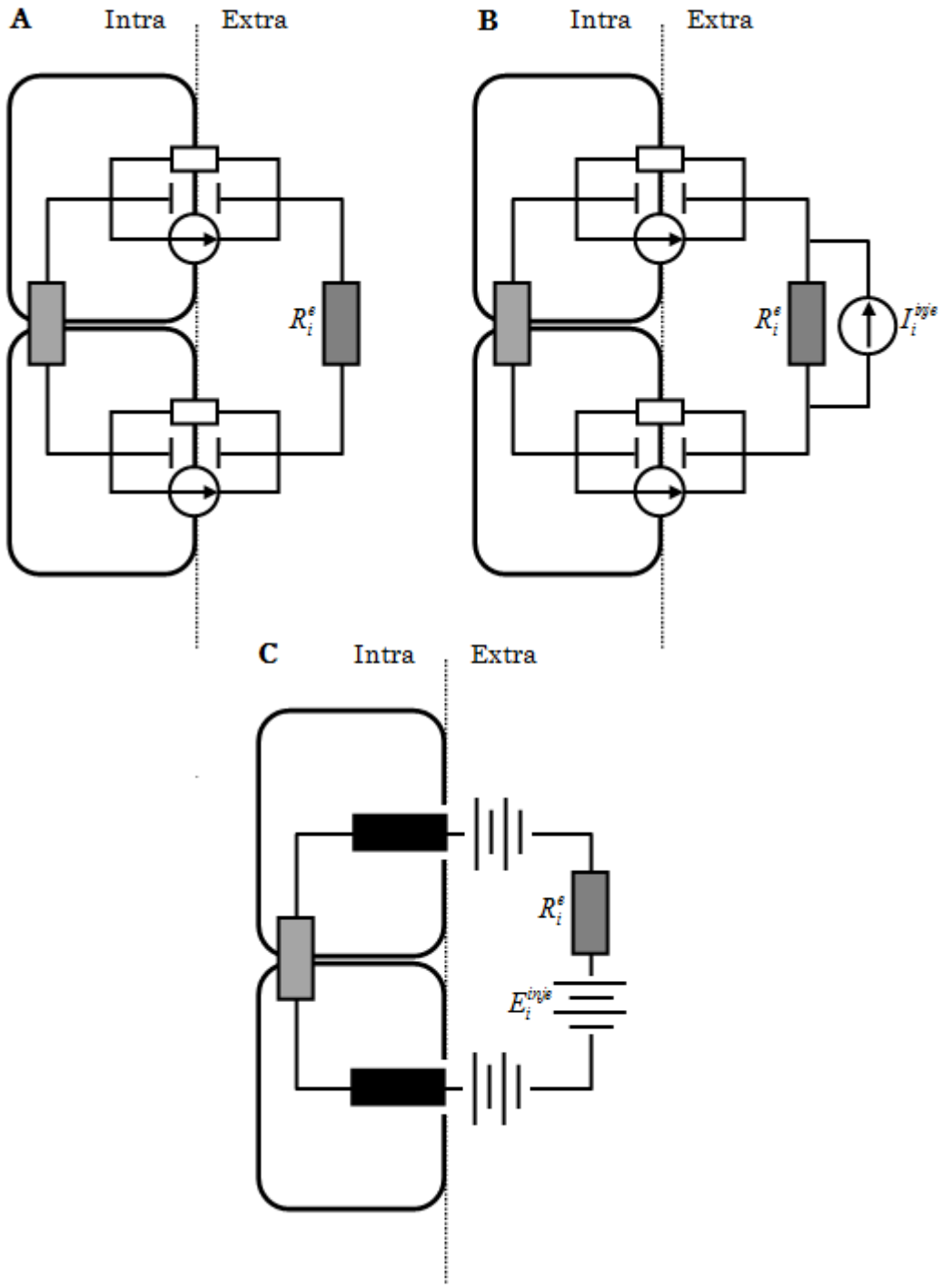
A
Intra
Extra
R_i^e
B
Intra
Extra
R_i^e
I_i^{inje}
C
Intra
Extra
R_i^e
E_i^{inje}

Figure 6

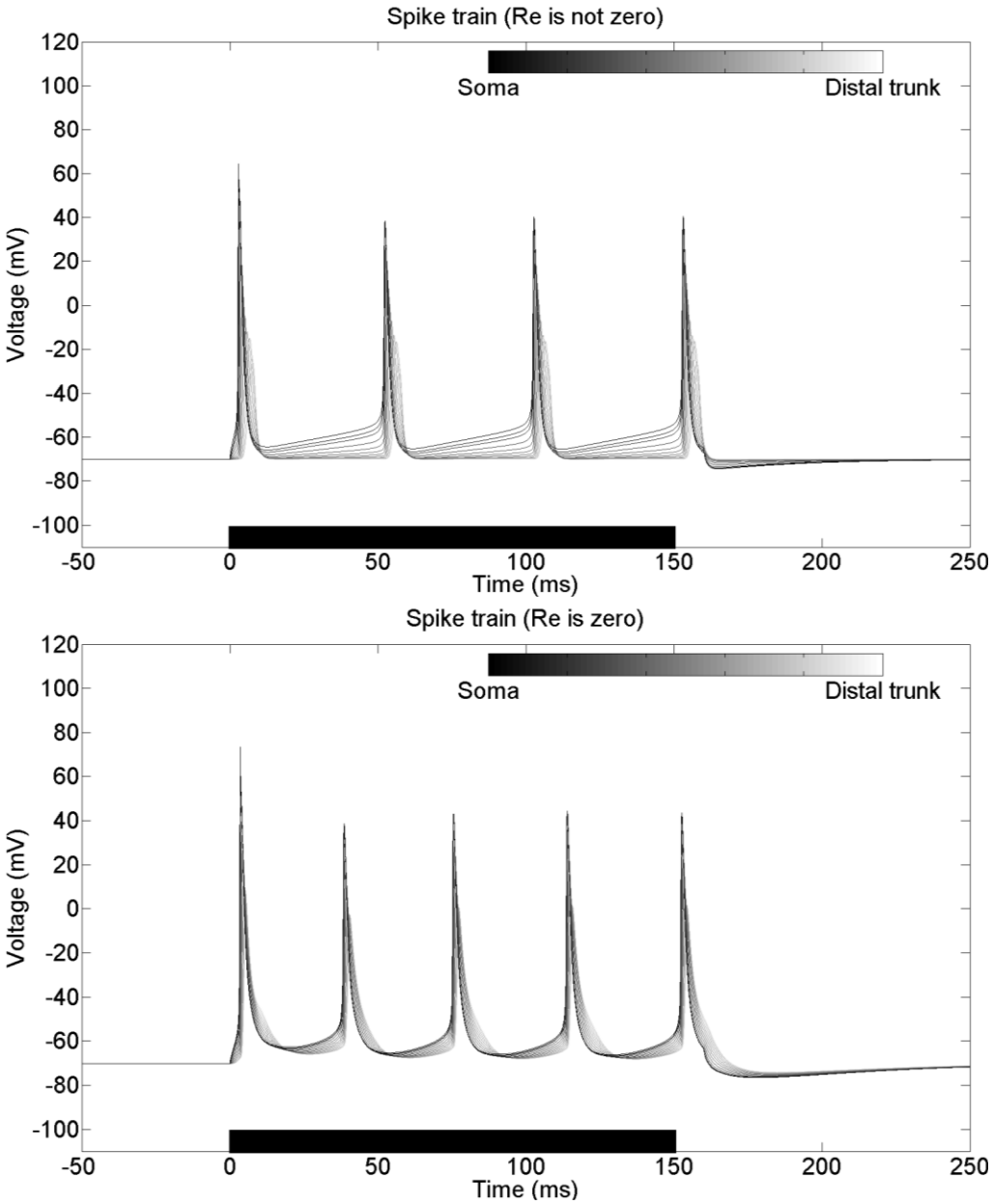
Spike train (Re is not zero)
Soma
Distal trunk
Voltage (mV)
Time (ms)
Spike train (Re is zero)
Soma
Distal trunk
Voltage (mV)
Time (ms)

Figure 7

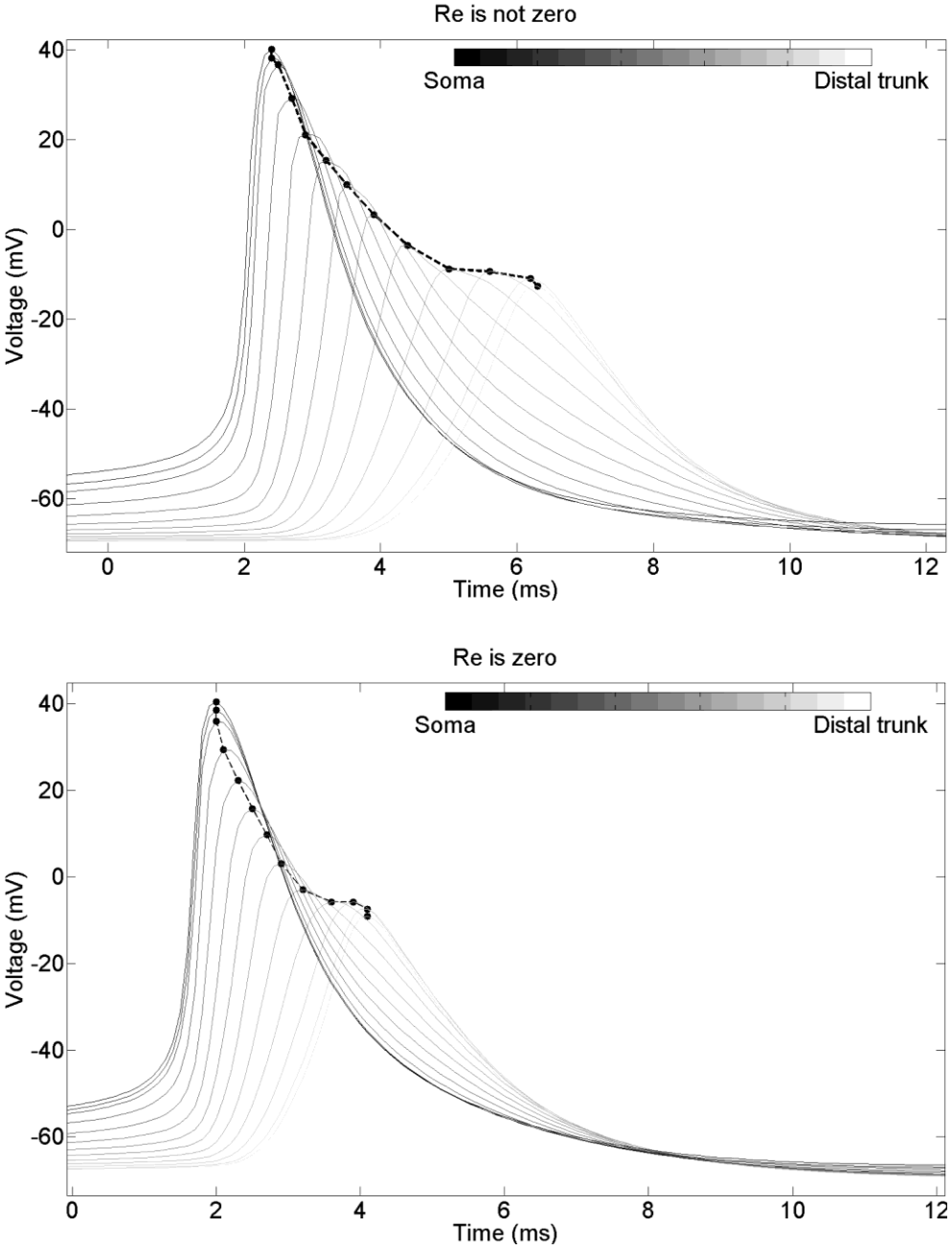
Re is not zero
Soma
Distal trunk
Voltage (mV)
Time (ms)
Re is zero
Soma
Distal trunk
Voltage (mV)
Time (ms)

Figure 8

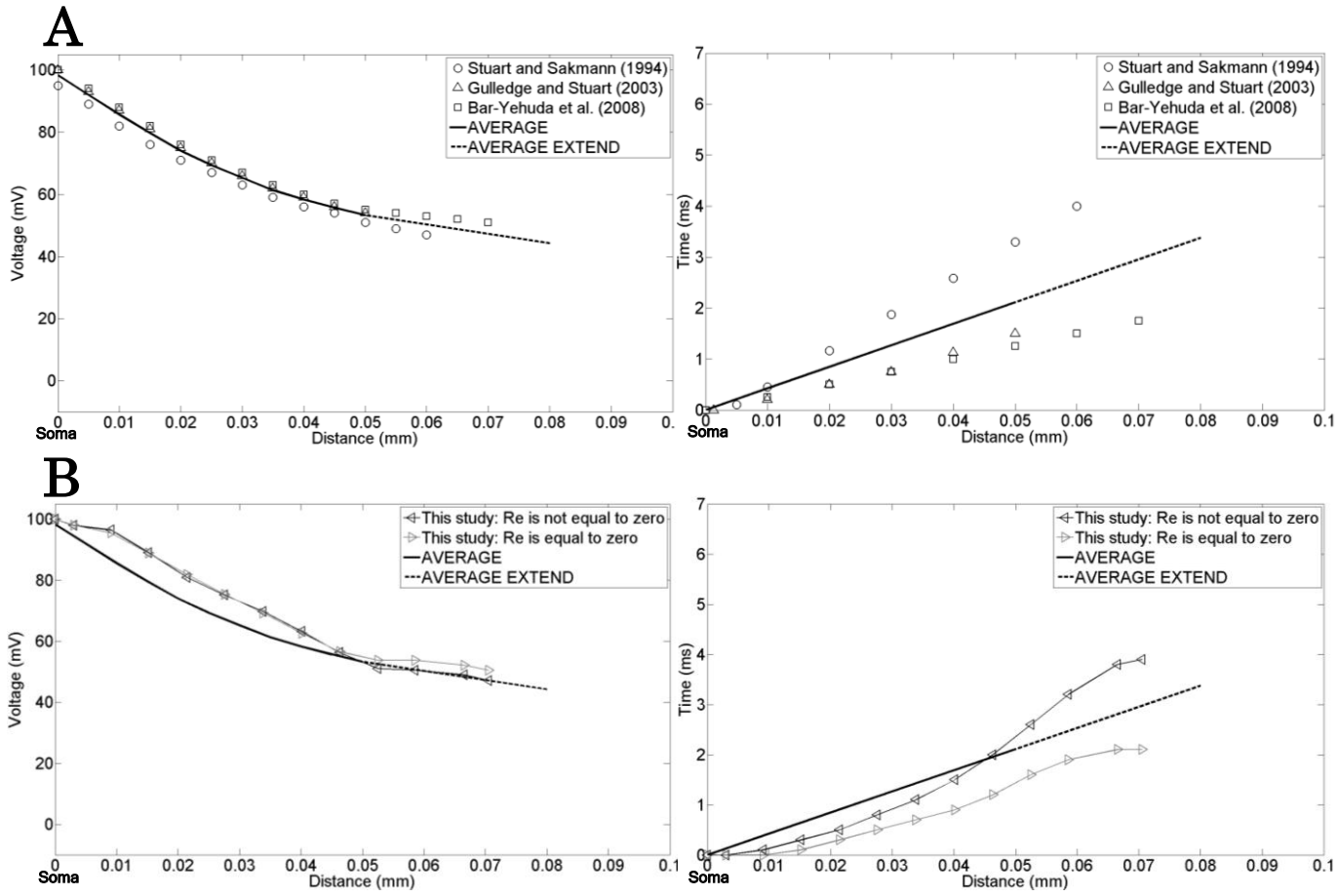
A
Stuart and Sakmann (1994)
Gulledge and Stuart (2003)
Bar-Yehuda et al. (2008)
AVERAGE
AVERAGE EXTEND
Voltage (mV)
Time (ms)
Distance (mm)
Soma
B
This study: Re is not equal to zero
This study: Re is equal to zero
AVERAGE
AVERAGE EXTEND
Voltage (mV)
Time (ms)
Distance (mm)
Soma

Figure 9

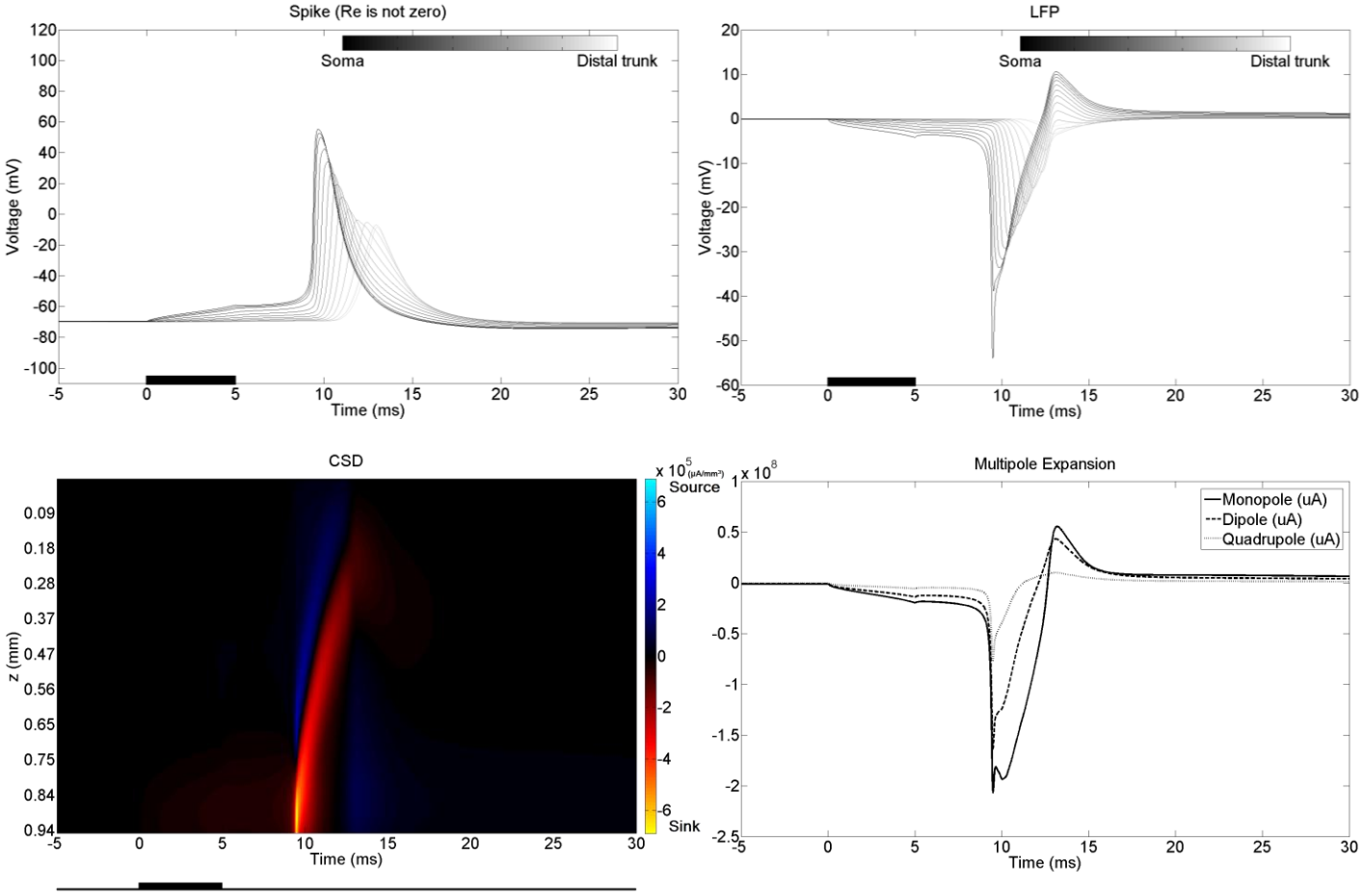
Spike (Re is not zero)
Soma
Distal trunk
Voltage (mV)
Time (ms)
LFP
Soma
Distal trunk
Voltage (mV)
Time (ms)
CSD
z (mm)
Time (ms)
x 10^5 (μA/mm³)
Source
Sink
Multipole Expansion
x 10^8
Monopole (uA)
Dipole (uA)
Quadrupole (uA)
Time (ms)

Figure 10

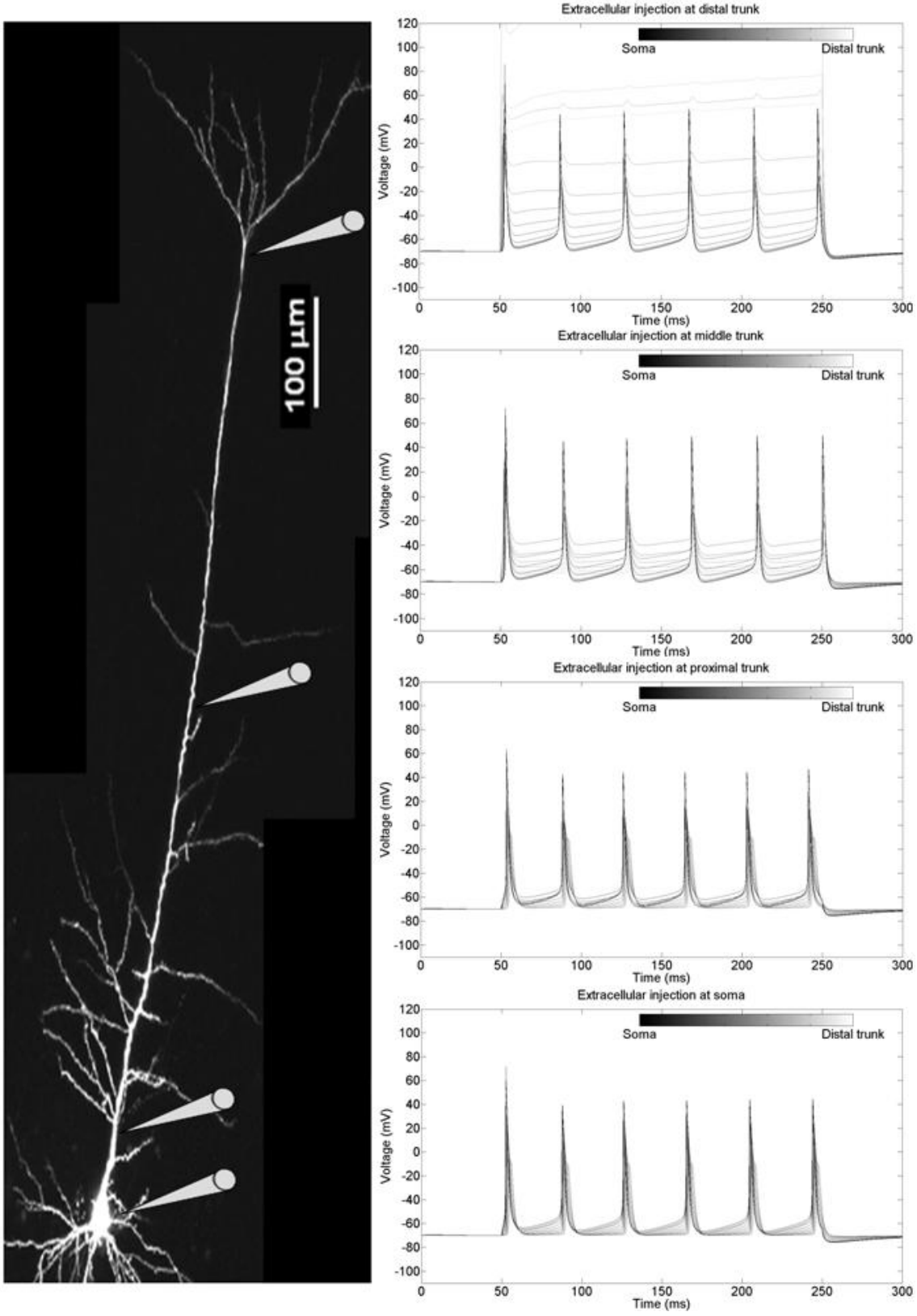
100 µm
Extracellular injection at distal trunk
Extracellular injection at middle trunk
Extracellular injection at proximal trunk
Extracellular injection at soma
Soma
Distal trunk
Voltage (mV)
Time (ms)

Figure 11

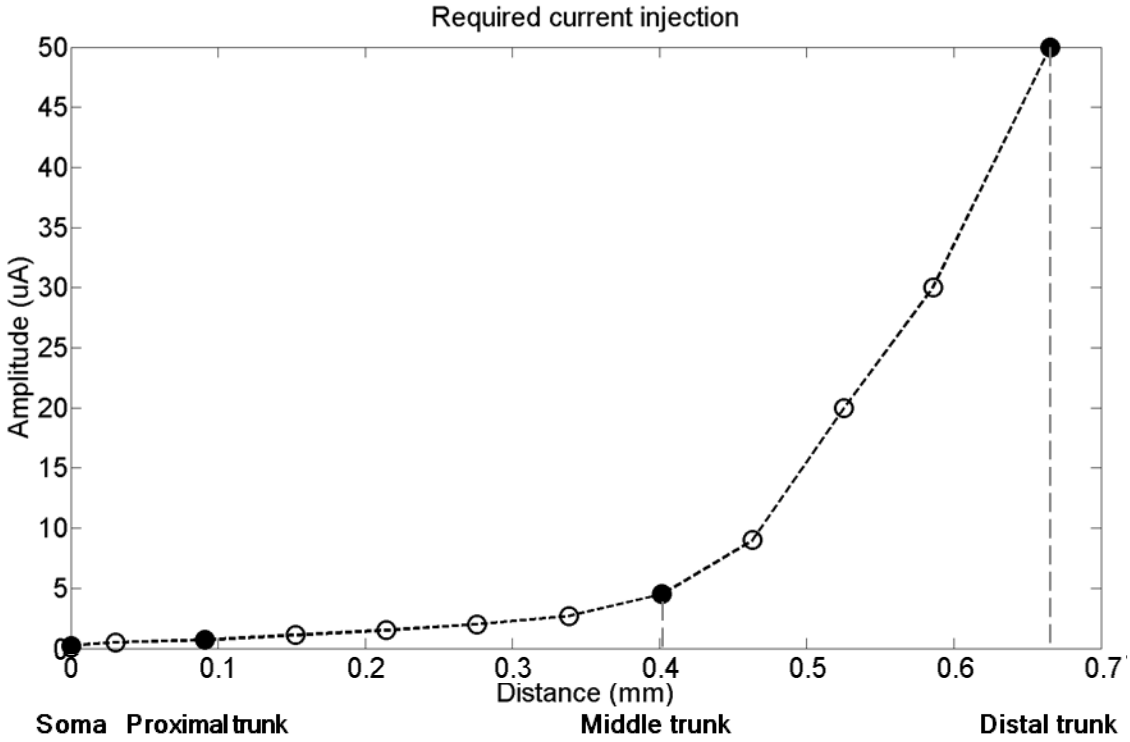
Required current injection
Amplitude (uA)
Distance (mm)
0
0.1
0.2
0.3
0.4
0.5
0.6
0.7
5
10
15
20
25
30
35
40
45
50
Soma
Proximal trunk
Middle trunk
Distal trunk

Figure 12

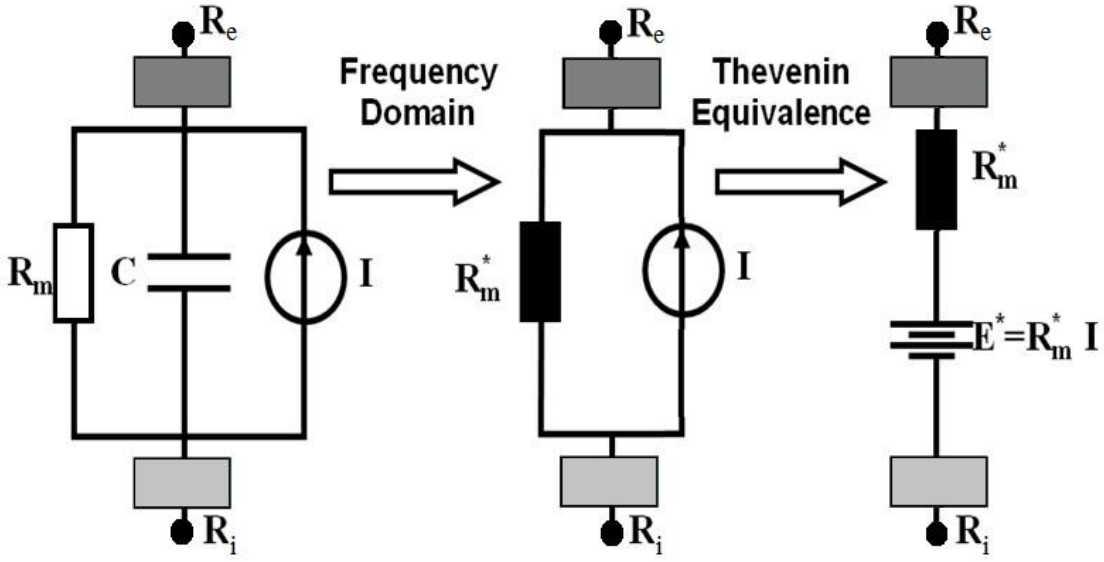
Re
Rm
C
I
Ri
Frequency Domain
Re
Rm*
I
Ri
Thevenin Equivalence
Re
Rm*
E*=Rm* I
Ri

Table 1

Integrator	**Length** MEAN±SD(μm)	**Diameter** MEAN±SD(μm)
Branch 1	205.89±25.00	1.26±0.05
Last Compartment	2.48±0.61	2.48±0.61
Propagator	**Length** MEAN±SD(μm)	**Diameter** MEAN±SD(μm)
Compartment 10	79.64±4.99	2.76±0.25
Compartment 9	60.47±7.68	2.69±0.55
Compartment 8	62.05±5.71	2.80±0.48
Compartment 7	61.66±8.69	2.71±0.38
Compartment 6	63.29±7.01	2.91±0.47
Compartment 5	62.51±7.44	3.01±0.79
Compartment 4	61.43±8.69	2.99±0.45
Compartment 3	61.93±6.68	3.05±0.45
Compartment 2	61.47±5.12	3.33±0.20
Compartment 1	60.66±9.06	4.34±0.46
		Diameter MEAN±SD(μm)
Collector		13.40±1.40